

MASTER OF SCIENCE PROGRAM
IN
EARTH OBSERVATION

Monitoring dynamics and sea-ice export of the
Southern West New Siberian polynya,
using model and remote sensing data

T. Krumpen

Promoter

Dr. C. Haas¹, Dr. W. Dierking¹, Prof. Dr. G. Govers², Prof. Dr. J. Harbor³



¹Alfred Wegener Institute for Polar and Marine Research, Busse Str. 24, 27570 Bremerhaven, Germany

²Physical and Regional Geography Research Group, K.U.Leuven,
Celestijnenlaan 200 E, 3001 Heverlee, Belgium

³Department of Earth and Atmospheric Sciences, Purdue University,
550 Stadium Mall Drive, West Lafayette, IN 47907-2051, USA

Bremerhaven, May 23, 2006

Content

List of abbreviations	3
1. Introduction	5
2. Data	8
2.1 <i>Acquisition and processing of ENVISAT ASAR data</i>	8
2.2 <i>AVHRR and AMSR-E data</i>	10
2.3 <i>Moorings</i>	11
2.4 <i>Weather data and bathymetry</i>	11
3. Sea-ice regime in the south-eastern Laptev Seas	12
3.1 <i>Deriving seasonal sea-ice parameters</i>	12
3.2 <i>Seasonal sea-ice variability</i>	13
3.3 <i>Microwave scattering evolution of the system</i>	17
3.4 <i>Polynya backscatter signatures</i>	19
4. Polynya evolution and ice production model	21
4.1 <i>Modelling polynya evolution</i>	22
4.1.1 <i>Polynya segmentation</i>	22
4.1.2 <i>Total polynya width reconstruction</i>	26
4.1.3 <i>Open water width reconstruction</i>	29
4.1.4 <i>Polynya area</i>	31
4.2 <i>Modelling ice growth</i>	31
4.2.1 <i>Open water heat budget</i>	31
4.2.2 <i>Frazil ice accumulation</i>	33
4.2.3 <i>Thin ice growth</i>	34
4.3 <i>Salt fluxes</i>	35
5. Polynya model results	37
5.1 <i>Sensitivity study</i>	41
6. Discussion	43
6.1 <i>Total polynya width algorithm</i>	43
6.2 <i>Open water width algorithm</i>	44
6.3 <i>Polynya length</i>	46
6.4 <i>Ice growth modelling</i>	46
6.4 <i>Ice and salt flux</i>	48
7. Conclusion and future direction	50
Acknowledgements	52
References	53
Appendix	57
A1. <i>Figure: Model work flow</i>	58
A2. <i>Table: Sensitivity study</i>	59

List of abbreviation

I) Text

<i>AARI</i>	Arctic and Antarctic Research Institute
<i>AL</i>	Anabar-Lena
<i>AMSR-E</i>	Adv. Microwave Scanning Radiometer - EOS
<i>APP</i>	Alternating Polarization Product
<i>ASAR</i>	Advanced Synthetic Aperture Radar
<i>AVHRR</i>	Advanced Very High Resolution Radiometer
<i>CTD</i>	Conductivity Temperature Depth meter
<i>GAC</i>	Global Area Coverage
<i>IBCAO</i>	Intern. Bathymetry Chart of the Arctic Ocean
<i>IST</i>	Ice Surface Temperature
<i>LAC</i>	Local Area Coverage
<i>NET</i>	North-Eastern Taimyr Polynya
<i>NOAA</i>	National Oceanic and Atmospheric Admin.
<i>NS</i>	New Siberian
<i>psu</i>	Practical Salinity Units
<i>OGCM</i>	Ocean General Circulation Models
<i>SAA</i>	Satellite Active Archive
<i>SAR</i>	Synthetic Aperture Radar
<i>SPM</i>	Suspended Particulate Matter
<i>SSM/I</i>	Special Sensor Microwave Imager
<i>SWNS</i>	southern West New Siberian Polynya
<i>T</i>	Taimyr
<i>WNS</i>	West New Siberian
<i>WSM</i>	Wide Swath Medium

II) Equations

a) Radar

<i>DN</i>	Image pixels value
β^0	Radar brightness
σ^0	Radar backscatter coefficient / sigma nought
<i>K</i>	Absolute calibration constant
α	Local incident angle

b) Modelling polynya evolution

<i>U</i>	Wind velocity (Dunai Station)
$A(\varphi_n - \varphi_o)$	Constant opening and closing factor
φ_n	Recorded wind direction (Dunai Station)
φ_o	Dominant wind direction for opening events
R_{OW}	Open water width
R_{TI}	Thin ice width
R_{total}	Total polynya width
Δt	Time interval between climate measurements
B_I	Thin ice drift velocity in percent of wind speed
b_I	Frazil ice drift velocity in percent of wind speed
Δh_f	Frazil ice production rate
h_c	Frazil ice accumulation depth
<i>l</i>	Polynya length
A_{OW}	Open water area
A_{TI}	Thin ice area
A_{total}	Total polynya area

c) Modelling ice growth

Q_T	Upward turbulent heat flux,
Q_L	Upward lw. radiation emitted by the sea,
Q_B	Downward lw. radiation absorbed at ocean surface
Q_S	Shortwave solar radiation.
Q_{net}	Surface net balance
T_a	Air temperature (Dunai Station)
T_s	Sea surface temperature
ρ_a	Air density
C	Heat transfer coefficient
σ	Stefan-Boltzmann constant
ϵ_s	Water surface emissivity
CL	Cloud cover
S_0	Solar constant
v_p	Vapour pressure
z	Sun zenith angle
ϕ	Latitude
τ	Solar hour angle
rH	Relative humidity
ρ_f	Frazil ice density
L_s	Latent heat of fusion for sea-ice
dH	Continuous thin ice growth in thin ice area
H	Ice thickness
h_s	Snow cover thickness
k_s	Thermal conductivity of snow
k_i	Thermal conductivity of ice
C_t	Net surface heat exchange
ρ_i	Ice density
Δh_f	Frazil ice production rate
h_c	Frazil ice accumulation depth

1. Introduction

[1] The Laptev Sea is a marginal sea of the Arctic Ocean and ranks foremost as a source of ice production among the wide Eurasian shelves. It is located between the coast of Siberia, the Severnaya Zemlya and the New Siberian Islands (Figure 1). The total area of the Laptev Sea comprises approximately $661.25 \times 10^3 \text{ km}^2$ [Bareiss *et al.*, 2005; Macdonald *et al.*, 2005; Dieckmann *et al.*, 2003]. Formation and growth of sea-ice in the Laptev Sea is dominated by ice production in coastal polynyas and flaw leads [Eicken *et al.*, 1997]. The ice regime in the eastern Laptev Sea is characterized by four features: Nearshore bottomfast ice, fast ice, pack ice and flaw polynyas, separating landfast ice from pack ice. According to Bareiss *et al.*, [2005] most of the eastern Laptev Sea surface is covered with ice from October to June. Based on their passive microwave radiometer-derived sea-ice concentration data from 1979 through 2002, sea-ice melting starts on average around July 4 (± 8.2 days), two months later a sea-ice minimum of $46 \times 10^3 \text{ km}^2$ is reached. New ice formation (freeze-up) starts at the end of September.

[2] The bottomfast ice develops in shallow parts, nearshore (depths less than 2 m). Although this feature is important on helping to maintain submarine permafrost in the spits and thus controlling

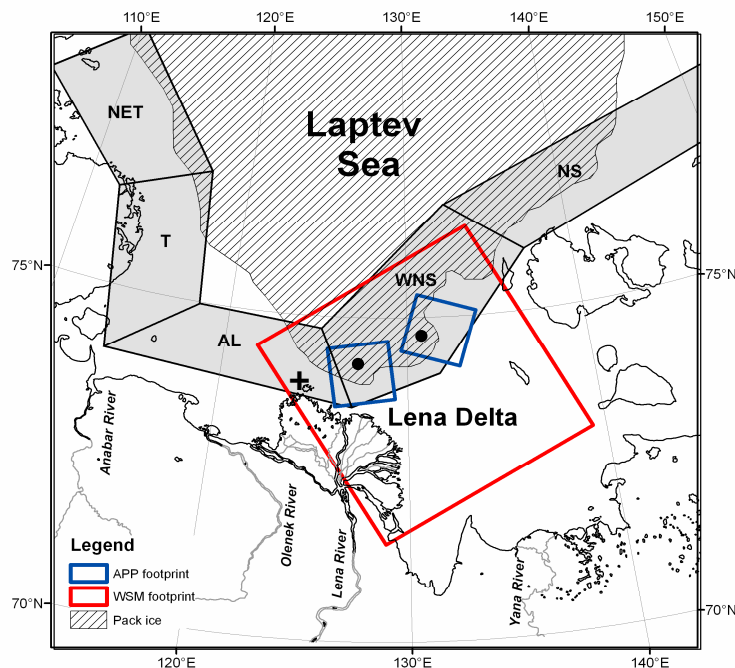


Figure 1. Map of the Laptev Sea showing the locations of main recurrent flaw polynyas (shaded boxes). Abbreviations are explained in the text. The typical WSM and APP coverage is indicated by frames (red for WSN and blue for APP). The mooring positions are marked by circles and the weather station by a black cross.

coastal morphology [Eicken *et al.*, 2005], so far it is not well understood. Floating fast ice, which reforms yearly, covers 50 % of the shallow eastern Laptev Sea and extends up to 200 km off the coast during winter. Bottom depth is the main factor determining the extent of fast ice coverage, that usually ends where the water reaches a depth of about 25 m. Beyond this level, ice ridges and other pieces of ice, protruding from the bottom of the ice cover, rarely remain aground. Drill hole measurements carried out in 1999 revealed an average fast ice thickness of 1.95 m in the southern Laptev Sea [Haas *et al.*, 2001a]. Freshwater fast ice adjacent to river mouths can grow up to 2.2 m [Dmitrenko *et al.*, 2005].

[3] The pack ice extent varies with ice import and export processes taking place in the Laptev Sea. Pack ice consists of ice originally formed as fast ice, but now dislodged from shore, and ice formed at sea. It can be flat over extensive areas, but also areas with a rough relief occur due to convergence of floes.

[4] Between fast ice and pack ice recurrent flaw polynyas are formed. A polynya is defined as a non-linear shaped opening enclosed in sea-ice. Sometimes the polynya is limited on one side by the coast (shore polynya) or by fast ice (flaw polynya) [World Meteorological Organization, 1970]. Polynyas which occur repeatedly at fixed geographic locations and during the same periods of the year are defined as recurrent polynyas [Martin, 2001]. Following Zakharov [1966], the prominent flaw polynyas in the Laptev Sea (Figure 1) are the New Siberian Polynya (NS), the West New Siberian Polynya (WNS), the Anabar-Lena Polynya (AL), the Taimyr Polynya and the North-Eastern Taimyr Polynya (NET). According to its geophysical mechanism and shallow bottom topography, the recurrent flaw polynyas in the Laptev Sea are classified as shelf water latent heat polynyas. Winter winds advect the pack ice away from the adjacent fast ice edge, so that large regions of open water are directly exposed to the cold air. The heat loss across the sea-air interface results in ice production, which is then continually driven away by currents and winds. Following the Steady State Model described in Pease [1987], the process that actually keeps this type of polynya open is the export of ice. The alongshore length of the Laptev Sea polynyas ranges from 100 km to 2000 km, the width from 1000 m to 100 km or in terms of area, from 10 to 10^5 km² [Barber *et al.*, 2001].

[5] Among the marginal seas of the Arctic Ocean, the Laptev Sea represents one of the most significant sites of net ice production. Flaw leads and polynyas produce as much as 20 % of the ice transported through the Fram Strait [Rigor *et al.*, 1997]. The intensive ice formation locally increases salinity of the water surface and induce convective mixing down to the seafloor, being an important source of saline shelf water for the Arctic Ocean [Winsor *et al.*, 2000, Bareiss *et al.*, 2005, Biggs *et al.*, 2003]. Based on long-term thermohaline records in the south-eastern Laptev Sea, Dmitrenko *et al.* [2005] studied the variability of the surface characteristics in the WNS polynya. However, the observed strong vertical density stratification in the polynya region and a convective

mixing probability of only 20 % implies that its contribution to saline shelf water formation is less than expected.

[6] So far, ice dynamics and ice export rates in the south-eastern Laptev Sea have received comparatively little attention. *Eicken et al.* [1999] investigated the interaction between river water and landfast sea-ice through SAR observations and ice growth modelling. *Rivera et al.* [2005] reconstructed the variability of freshwater discharge to the Arctic via the Lena River. The comprehensive study of *Bareiss et al.* [2005], presented sea-ice dynamics in the entire Laptev Sea during 24 years from 1979 through 2002 and linked the detected variability to the large-scale atmospheric circulation. Nevertheless, accurate satellite based calculations of ice and salt flux in the south-eastern Laptev Sea are still missing. The few existing studies are based on passive microwave satellite data. Nevertheless, sensor characteristics of the passive microwave radiometer and deficiencies in the used sea-ice concentration algorithms that discriminate unambiguously between thin ice and open water, limit the accuracy of the obtained results.

[7] In recognition of its importance, the WNS polynya has been the subject of several Russian-German research projects in the framework of studies of the Laptev Sea system [*Haas et al.*, 2004a]. To examine ice thickness variations, surface circulation regime, salinity and water temperature changes in the WNS polynya, two moorings were deployed in the water body close to the fast ice edge. In parallel, ENVISAT Advanced Synthetic Aperture Radar (ASAR) images were acquired for the period between October 2003 and June 2004 to monitor the evolution of the southern WNS (SWNS) polynya. Wide Swath Medium (WSM) resolution image products cover the position of the sea floor observatories and the Lena Delta, while Alternating Polarization Mode products (APP) map the region around the moorings with higher spatial resolution. Figure 1 presents a map of the Laptev Sea, showing the locations of the most prominent flaw polynyas and typical frames of WSM (red) and APP (blue) images.

[8] Our objective is to model the amount of ice produced and brine rejected in the SWNS polynya in winter 2003/2004. Therefore we applied an approach developed by *Haarpaintner et al.* [2001] that simulates the polynya evolution in time based on meteorological records and satellite observations. The polynya model reconstructs the evolution of thin ice and open water fraction, separately. Using algorithms for frazil ice production in open water and ice growth in thin ice regions, the total ice production and salt flux is calculated. Since the accuracy of the open water model developed by *Haarpaintner et al.* [2001] is rather weak, we evaluate three slightly different approaches. The implementation of tidal forcing and freeze-up events into the open water width model is treated in this study. Furthermore we demonstrate the potential of cross-polarization ratios and AVHRR/ASAR composites for automatic polynya segmentation. Finally, the modelled increase in water salinity is

compared to the long-term average salinity variance measured by *Dmitrenko et al. [2005]*. This provides information about the model accuracy and supports the interpretation of field records.

[9] This dissertation is structured as follows: Section 2 describes the obtained satellite, climate and mooring data and section 3 deals with the general sea-ice regime and the microwave scattering evolution of the south-eastern Laptev Sea, derived from ENVISAT ASAR data. Section 4 introduces the applied polynya model and algorithms used for ice growth calculations. Section 5 presents results of the modelling approach and examine their sensitivity to meteorological input data and ice partition parameters. Section 6 discusses our observations, explains the necessity for further improvements, and links the results to earlier studies. Section 7 gives our conclusions.

2. Data

2.1 Acquisition and processing of ENVISAT ASAR data

[10] The acquired 45 VV-polarized¹ WSM ENVISAT ASAR scenes cover the Lena Delta and the southern part of the WNS polynya (50 % of the entire WNS polynya) between October 2003 and June 2004. The swath width is approximately 400 km with a resolution of 150 m. Scenes were obtained on either ascending (around 12 am) or descending (around 2 am) orbits. The mooring positions were mapped with 34 APP images. APP products consist of two simultaneously acquired images (VV- and HH-polarization), with a swath width of 100 km and a spatial resolution of 30 m. On average, WSM images could be obtained 0.9 times a week. The temporal coverage of APP is less, due to a lack of satellite ground station visibility. Image acquisition dates are given in Figure 3e.

[11] The potential of radar for sea-ice mapping and general SAR principles are discussed in *Kaleschke [2003]*, *Mahafza [1998]*, *Hall [1985]* and *Massom [1991]*. A comprehensive view of the SAR imaging geometry, external and internal radiometric calibration and backscatter models for different sea-ice types are given in *Small et al. [2005]*, *Kaleschke [2003]*, *ESA [1993, 2004a]*, *Ulaby et al. [1986]* and *Sandven et al. [1999]*.

[12] ASAR level 1 products are delivered without geometric and radiometric calibration. The radiometric calibration of ENVISAT scenes was carried out with the ESA software B.E.S.T (Basic

¹ Polarisation refers to the orientation of the plane of the electric field in conventional imaging radar systems. The ENVISAT ASAR system is designed to transmit either vertically polarised or horizontally polarised radiation. This means that the electric field of the wave is in a vertical plane or a horizontal plane. Likewise, the radar can receive either vertically or horizontally polarised radiation. Thus the polarisation of a radar image can be *HH*, for horizontal transmit, horizontal receive, *VV* for vertical transmit, vertical receive, *HV* for horizontal transmit vertical receive, and vice versa (*VH*) [ESA, 2004b].

ENVISAT SAR Toolbox). The relationship between the image pixels value (DN), the radar brightness (β^0) and the radar backscatter coefficient² (σ^0) for ASAR level 1 products is expressed as:

$$DN^2 = K \cdot \beta^0 = K \cdot \frac{\sigma^0}{\sin(\alpha)} = K(\alpha) \cdot \sigma^0, \quad (1)$$

where K is the absolute calibration constant and α is the local incident angle. According to *ESA* [2004a], K is based on measurements over precision transponders and varies with processor and product type and might eventually also change between different beams for the same product. Calibrated sigma nought and gamma images for WSM and APP products can be derived by:

$$\sigma^0_{i,j} = \frac{DN^2_{i,j}}{K} \sin(\alpha_{i,j}), \quad (1.1)$$

$$\gamma_{i,j} = \frac{\sigma^0_{i,j}}{\cos(\alpha_{i,j})}, \quad (1.2)$$

Finally sigma nought is converted to dB by:

$$\sigma^0 [dB] = 10 \cdot \log_{10}(\sigma^0), \quad (1.3)$$

The geometric registration (using the provided geolocation grid information stored in the header) is based on standard methods. All scenes were geocoded to an UTM projection.

[13] The ASAR images and WSM products in particular, show large variations of σ^0 across the full swath for most surfaces, because returns due to surface scattering are normally strong at low incidence angles and decrease with increasing incidence angle, with a slower rate of decrease for rougher surfaces [ESA, 2004b]. For visual image interpretation, comparison and presentation, the effect of the incident angle on sigma nought was eliminated by a so called Range-Normalization procedure. Following *Sandven* [2000], we applied a pre-defined range-normalization function to all scenes:

² Scattering coefficient, or the conventional measure of the strength of radar signals reflected by a distributed scatterer, usually expressed in dB. It is a normalised dimensionless number, comparing the strength observed to that expected from an area of one square metre. Sigma nought is defined with respect to the nominally horizontal plane, and in general has a significant variation with incidence angle, wavelength, and polarisation, as well as with properties of the scattering surface itself [ESA, 2004].

$$DN_{RN} = (\sigma^0) \cdot \tan(\alpha)^\beta, \quad (1.4)$$

For fast ice and pack ice in ASAR images we found $\beta = 1.8$ to give overall good results (see Figure 2, before and after range-normalization). To eliminate incident angle effects over large open water regions, we used 5.2 for β . A flow diagram of the automated calibration procedure for ENVISAT ASAR products is given in Figure 2.

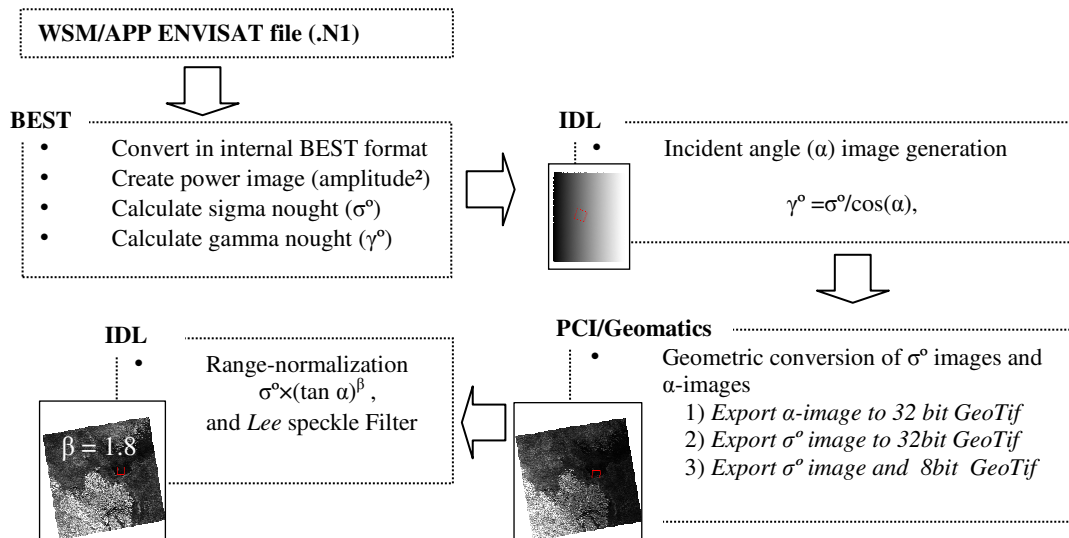


Figure 2. Flow diagram of automated radiometric and geometric radar image calibration.

2.2 AVHRR and AMSR-E data

[14] For each WSM acquisition date, an Advanced Microwave Scanning Radiometer - EOS (AMSR-E) and an Advanced Very High Resolution Radiometer (AVHRR) scene were obtained. AMSR-E is a passive-microwave radiometer aboard Aqua. Sea-ice concentration is calculated using the ARTIST (ASI 5) sea-ice algorithm, which is freely available at the University Bremen (<http://iup.physik.uni-bremen.de:8084/amsr/amsre.html>).

[15] Under cloud free conditions, AVHRR aids radar image interpretation. Global (GAC) and Local Area Coverage (LAC) AVHRR data at visible- (channel 1) and infrared- (channel 5) wavelengths was downloaded from the NOAA Satellite Active Archive (SAA) and processed with TeraScan software by the University of Trier (<http://klima.uni-trier.de/>).

2.3 Moorings

[16] Two moored oceanographic bottom observatories were deployed on the Laptev Sea shelf for a one-year period (August 31, 2003 to September 15, 2004). Objective of the investigation was to monitor seasonal variations in currents and suspended particulate matter (SPM) and their implications for sediment transport and budget calculations and to relate them to polynya processes (Wegener *et al.*, 2005). Both bottom moorings were deployed beneath the fast ice edge at a depth of 25.4 m and 28.5 m, respectively. The locations of the bottom mooring stations (Lena: 74°07'N, 126°25'E and Yana: 74°31'N, 130°19'E) are marked in Figure 1 with solid circles.

[17] A mooring system consists of an Acoustic Doppler Current Profiler (ADCP) and a Conductivity Temperature Depth meter (CTD). ADCPs transmit sound pulses, propagating through the water column. The received backscatter intensity at the transducer enables to measure SPM concentrations and provides information about the ice thickness above the mooring. ADCP measurements were carried out at 1 min intervals and averaged over 30 min. The recorded distance between surface and pulse transmitter over time is plotted in Figure 3d. In addition, the ADCP provides data on current speed and direction and temperature at different depths. A description of the mooring setup is given in Wegener *et al.* [2005]. Ice thickness retrieval from ADCP and associated errors are discussed in Shcherbina [2002]. Unfortunately, rough sea-ice conditions caused the entire westerly mooring Yana and the salinity measurement device of mooring Lena to fail.

2.4 Weather data and bathymetry

[18] The meteorological data were provided by the Arctic and Antarctic Research Institute (AARI) in St. Petersburg, Russia, and are presented in Figure 3a, b and c. The weather station on Dunai Island, indicated as a black cross in Figure 1, recorded wind direction, wind velocity, air temperature and sea level pressure in 6-hour intervals. The station is located 50 km and 180 km away from the seafloor observatories, respectively.

[19] Bathymetry data are freely available for the entire Arctic on the NOAA IBCAO homepage (<http://www.ngdc.noaa.gov/mgg/bathymetry/arctic/arctic.html>). Data were masked to the study area and contour lines extracted in 5 m intervals.

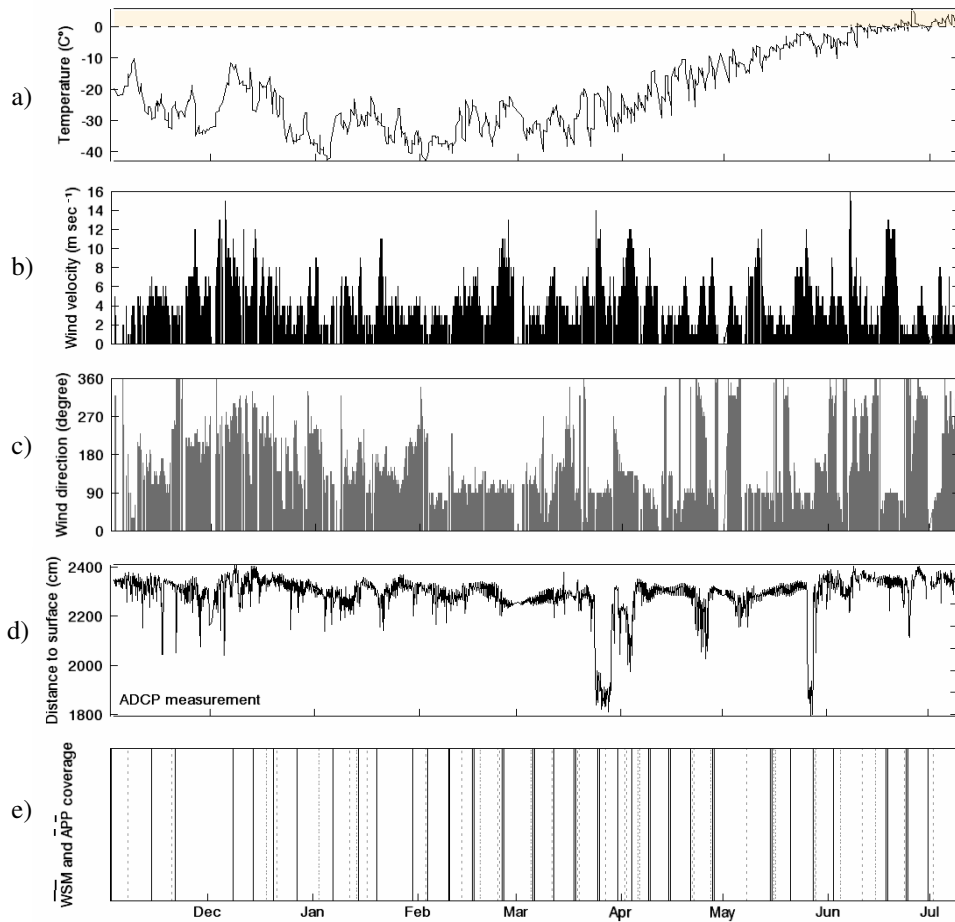


Figure 3. Meteorological data recorded at the Dunai Station: a) is air temperatures, b) wind direction and c) wind velocity and d) is ADCP derived distance between ice/water and transmitter. Lines in 2e) show the dates of WSM (solid) and APP (dotted) coverage.

3. Sea-ice regime in the south-eastern Laptev Sea

3.1 Deriving seasonal sea-ice parameters

[20] Figure 5 shows a set of calibrated WSM ASAR images, geocoded to UTM projection, acquired between November 14, and June 24. For presentation and to support image interpretation, the radar scenes have been speckle-reduced (*Lee* speckle filter, 3×3 kernel) and range-normalized by equation 1.4 with $\beta = 1.5$. To obtain a general insight of how the sea-ice regime of the Lena Delta develops in time, several sea-ice parameters have been extracted manually from the time-series. Tracking single prominent ice floes at a spatial sampling rate of 50×50 km on two sequential images,

visualizes the ice drift regime. The temporal sampling rate is between 7 and 10 days and the accuracy of tracked positions equal to the pixel size. The drift arrows in Figure 6 represent the ice movements between image pairs. The lower end of an arrow indicates where a tracked feature originally came from and the arrowhead where it drifted to. In addition to sea-ice drift, fast ice extent and grounded ice floes were mapped (indicated by the orange lines). Based on the ice tracking approach a number of statistics, such as mean sea-ice drift velocity and direction, were derived. A linkage of the sea-ice drift parameters to meteorological forcing shows that the ice drift direction in the Laptev Sea is mainly governed by wind direction. Figure 4 plots the observed wind direction averaged between two image dates over the observed mean sea-ice drift extracted from image overlap. The correlation coefficient r is 0.77. The agreement between recorded wind velocity and ice drift velocity is less ($r = 0.4$), since ice drift distance is strongly affected by the presents of grounded ice or fast ice in track direction and varying drift-resistances in open water, thin ice and pack ice zones. The high correlation coefficient between wind direction and drift direction suggest that the Dunai weather station is representative for the northern Lena Delta and the SWNS polynya. The correlation between ice movement and ocean current information recorded by the seafloor mooring is rather poor.

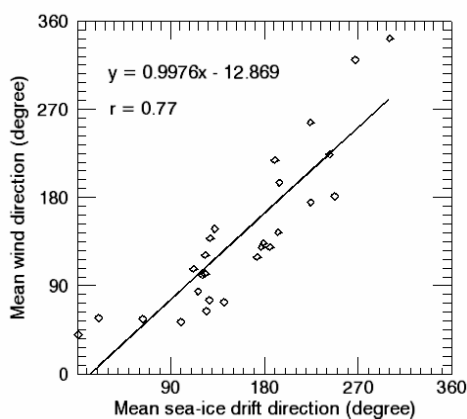


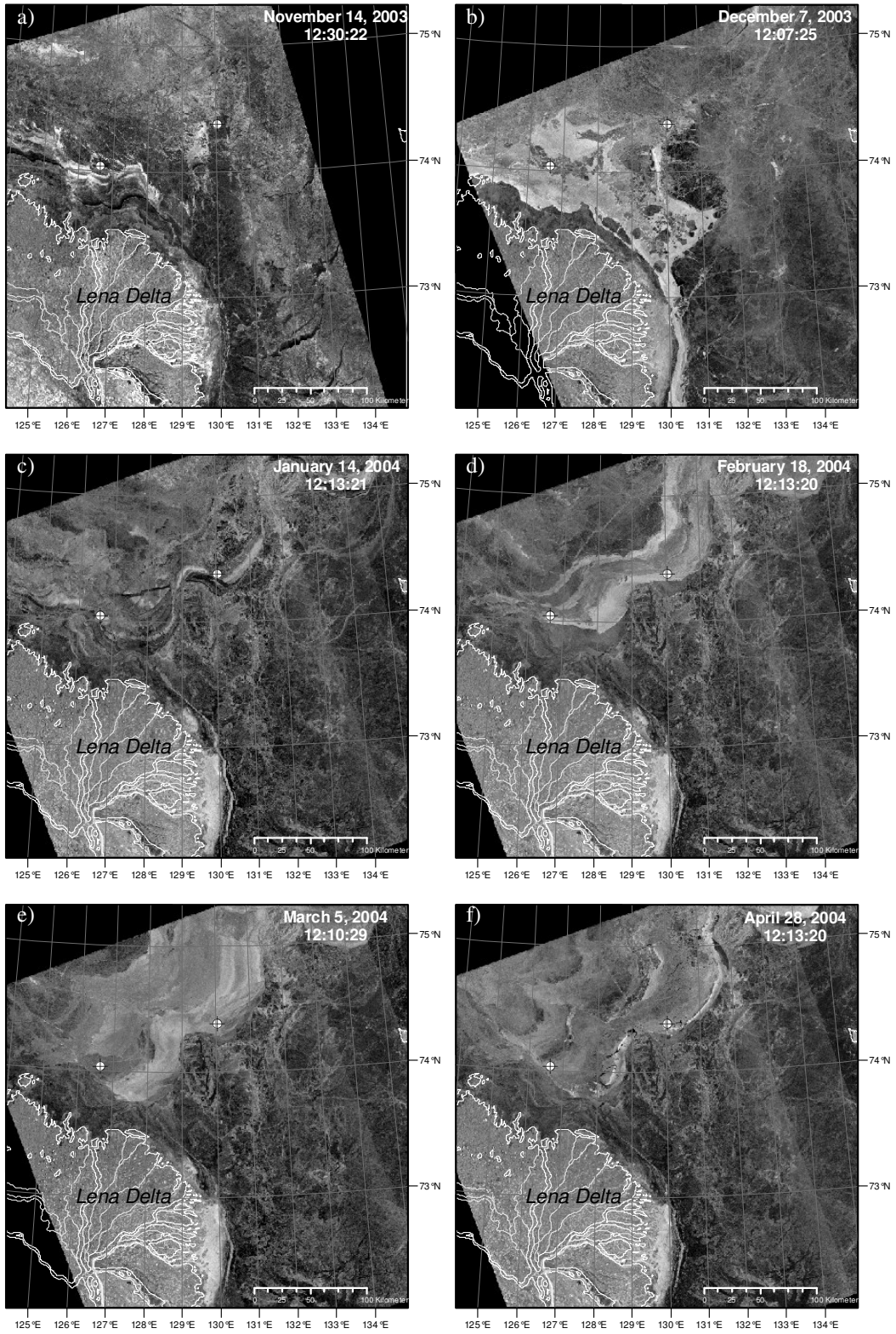
Figure 4. Mean wind direction, recorded at the Dunai weather station between two adjacent image dates, over mean sea ice drift direction, extracted from image overlap.

3.2 Seasonal sea-ice variability

[21] The interpretation of the ASAR images is supported by wind and air temperature records and sea level pressure data, obtained at the Dunai weather station in winter 2003/2004. From October 2003 on, the recorded temperatures continuously decreased until a minimum of -40°C was reached in early January (Figure 3a). Temperatures remained around -30°C to -40°C throughout the winter and rose only slowly in April. The temperatures exceeded freezing point of sea water (-1.8°C) first time in

the beginning of June. This threshold marks the change from a positive to a negative atmosphere-ocean heat budget and indicates the end of the ice production period. The wind regime is presented in Figure 3b. As discussed later, the wind directions revealed two main wind regimes [Haas *et al.*, 2004a]. Between October and end of January, the histogram peaked at 180° (southerly winds), while in the second half of winter winds prevailed at 90° (easterly winds). The average wind speed recorded at the weather station is around 4.3 m sec⁻¹. In addition to climate data, the seafloor mooring aids image interpretation, since continuous single point information about ice thickness supports ice type classification.

[22] According to passive microwave observations [Bareiss *et al.* 2005], freeze-up in the south-eastern Laptev Sea starts on September 25 (\pm 8.5 days). 2-3 weeks after temperatures dropped below 0°C, ice formation commences in the coastal shallow waters of the south-eastern Laptev Sea. In November, most of our study area is covered with a freely floating first-year ice cover and partially grounded fast ice. Convective mixing induced by strong winds in October/November quickly cooled the water body and accelerated ice formation in shallow parts. An ASAR image taken on November 14, (Figure 5a) shows that a narrow fast ice cover has established along the southern shelf. Ice formation is speeded up by river discharge that lowers the water salinity. In the first 3 weeks of November, a narrow band of high-backscatter ice develops along the coast, mostly confined to the area adjacent to the main river channels, which account for between 80% and 90% of the total Lena discharge. The band closely follows the 10 m isobaths and is coincident with regions of low salinity (0.1‰) [Eicken *et al.*, 2005]. In the region of our westerly mooring, banded structures indicate spots of ice production and the existents of a small coastal polynya. A period of strong persistent winds led to a partial break up of the fast ice cover [Haas *et al.*, 2004a] between end of November and mid of December. Ice was advected north-eastward (Figure 6b), so that a large coastal polynya can be seen along the fast ice edge in Figure 5b. Wind roughened open water surface with Langmuir strike (see section 3.4) are visible throughout the scene. This event shows that a stable fast ice cover does not develop before the middle of December [Haas *et al.*, 2004a]. Break up events are expected to play an important role for sediment transport and sea-ice formation in the south-eastern Laptev Sea [Wegener *et al.*, 2005; Reimnitz *et al.*, 1994]. Strong winds accompanied by low air temperatures supercool the entire water column and speed up the re-freezing process. In addition, high drift rates contribute to grounding and deformation of the freely floating first-year ice, which leads to the development of a large grounded area over a shallow bank southwest of the elliptical shaped island (Figure 6c). During the next 4 weeks, the distribution of fast ice hardly changed. Prevailing southern winds push the ice northward out of the delta (Figure 6d and 6e). A small peak in the bottom topography (10m depths) at 129.15° E and 74.15° N, close to the 25m isobaths, acts as a cork. A grounded small ice flow, which was already immobile from the very beginning, rapidly increases in



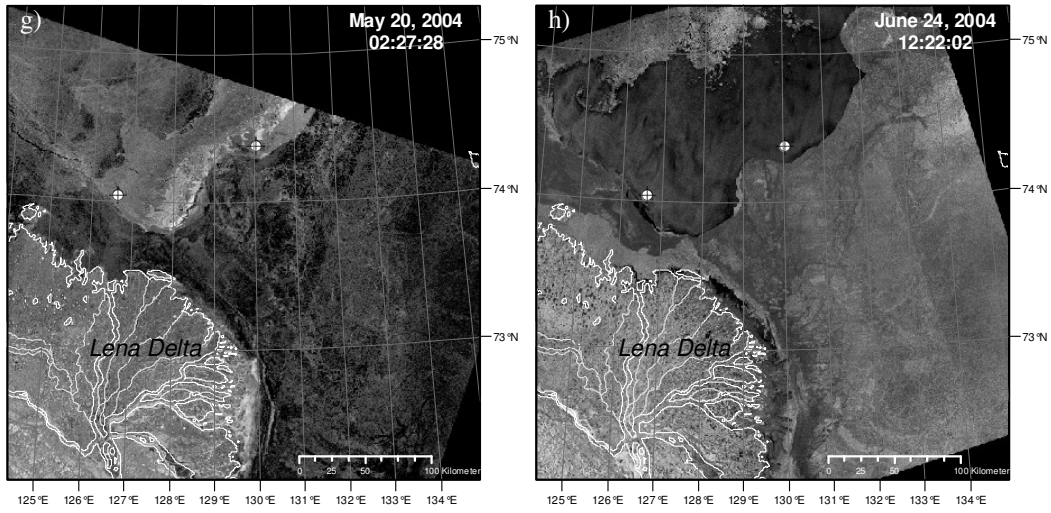
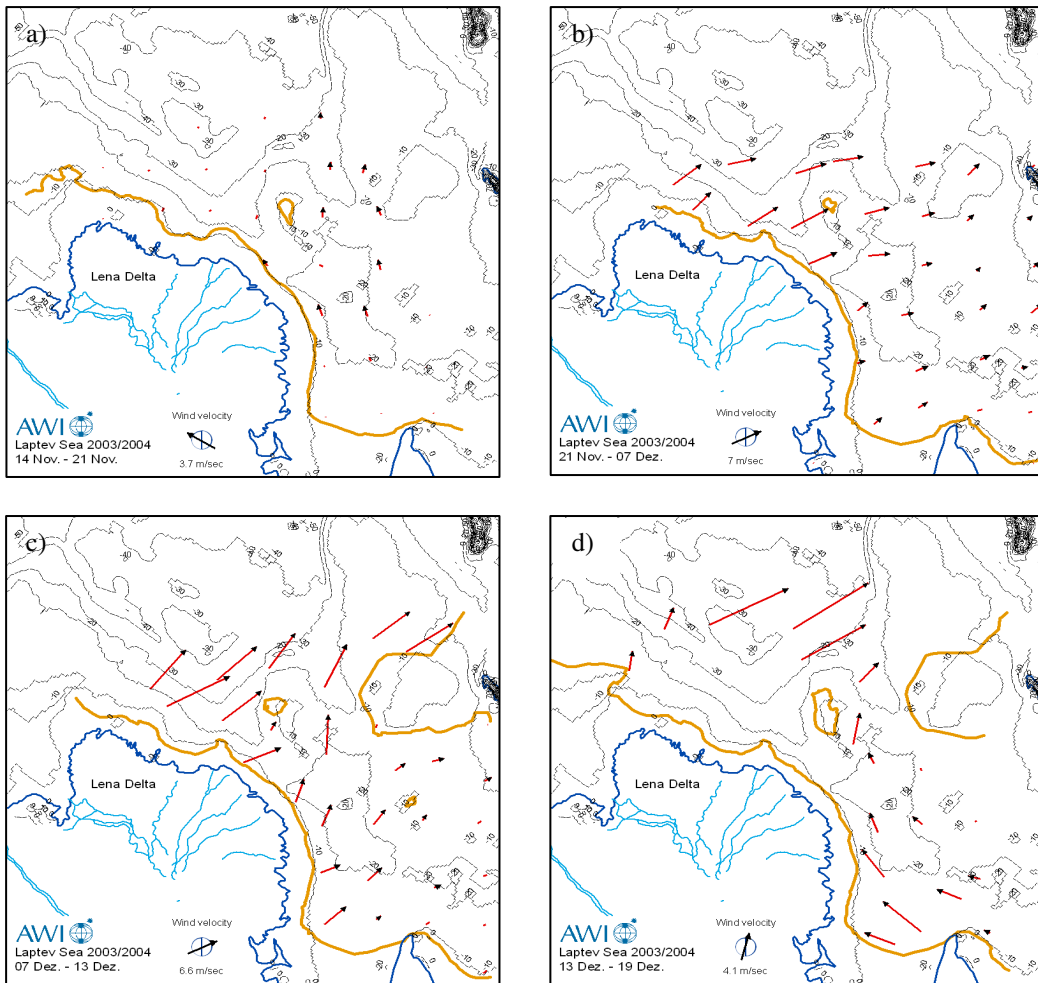


Figure 5. Time-series of ASAR-VV WSM images between November 2003 and June 2004. Images are calibrated and range-normalized.



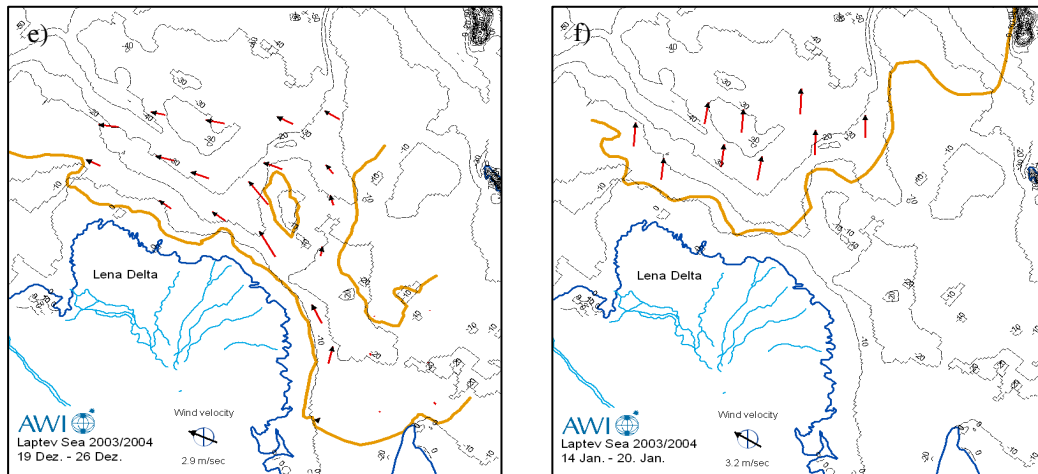


Figure 6. Sea-ice drift (arrows) and fast ice extend (orange lines) during the freeze-up period. Recorded mean wind velocity and direction between image pairs is plotted in the lower left.

size, until ice export out of the southern shallow regions stops. On January 14 (Figure 5c and Figure 6f), the fast ice cover is finally fully developed, but the break-up events have left it homogeneous.

[23] From January on, the fast ice edge closely followed the 25 m depth contour. As discussed by *Dmitrenko et al.* [1999], the landfast ice extent in the south-eastern Laptev Sea is linked to the dispersal of river freshwater prior to fall freeze-up through its impact on thermohaline circulation and stabilization of the ice cover. Therefore, large interannual differences in landfast ice extend can be observed [*Eicken et al.*, 2005; *Bareiss et al.*, 2005]. Between fast ice and seaward drift ice, zones of ice-free water or young ice are formed. Opening and closing of the SWNS flaw polynya varies in time and is mainly driven by wind directions and wind velocities. Section 4, 5 and 6 discuss the polynya dynamics and sea-ice export in the southern part in detail, using a polynya flux-model. Figure 5 d, e, f, g and h show different stages of the southern SWNS polynya in February, March, April, May and June.

3.3 Microwave scattering evolution of the system

[24] The strength of the backscattered signal increases until the end of December and varies only slightly across the winter. Recent research results have shown that a distinct pattern exists for the seasonal evolution of the microwave scattering coefficient over various sea-ice types [*Barber et al.*, 2000; *Drinkwater*, 1989; *Eicken et al.*, 2005]. Phenomenological patterns in the σ^0 cycle of sea-ice features vary with the dielectric properties of the material, incident angle, frequency and sensor polarization [*Belchansky et al.*, 2004]. To demonstrate the capability of the seasonal microwave scattering evolution for measuring geophysical and thermodynamic sea-ice states, we routinely

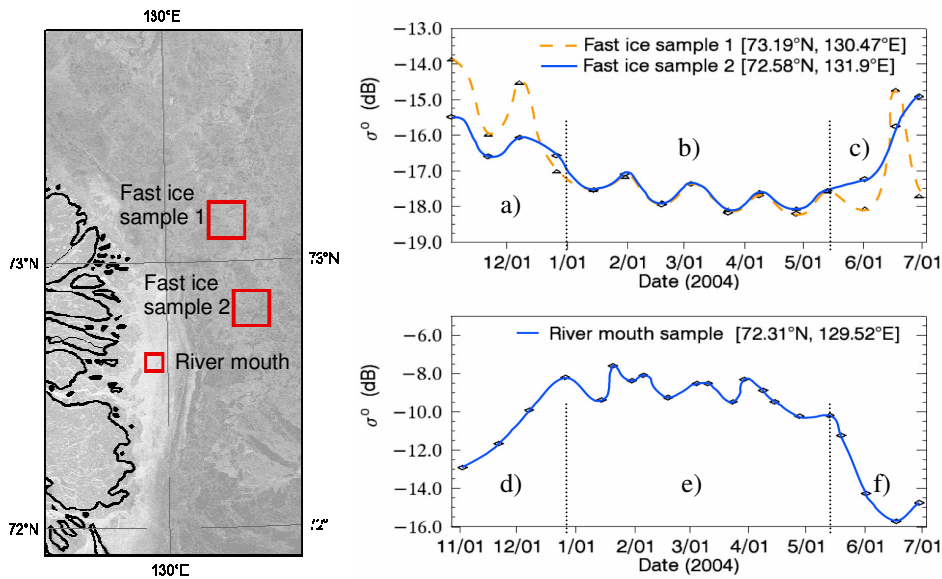


Figure 7. Seasonal evolution of σ^0 at 5.3 GHz (based on ENVISAT data) for fast ice (15 images at incident angle 30°) and river mouth ice (21 images at incident angle 33°). Backscatter was extracted at sample locations specified in the left image. A description of the seasonal sigma nought evolution is given in the text.

extracted backscatter time-series at different sampling points for fixed incident angles. A fixed incident angle geometry means, that observed changes in σ^0 can be attributed solely to changes in the dielectric properties of the material and not to imaging angle [Yackel *et al.*, 2000]. For demonstration, the σ^0 evolution of fast ice and ice adjacent to the river mouth is presented below:

[25] The upper right panel in Figure 7 presents the backscatter evolution of fast ice in WSM imagery at two different sample points. The mean σ^0 was calculated over a 150×150 pixel kernel. Following Livingstone *et al.* [1987], the phenomenological σ^0 cycle can be classified in freeze-up-, winter-, early melt- and melt onset periods. The freeze-up period for fast ice is characterized by high amplitude of microwave scattering (Figure 7a). The presence of frost flowers temporarily strengthens the received signal, until snow deposition in mid December reduces scattering and breaks down the frost flower effect [Barber *et al.*, 2000]. During winter period (Figure 7b, January to May) the microwave backscatter oscillates only slightly. Following Yackel *et al.* [2000], the oscillation is driven by atmospheric forcing of the snow/ice interface temperature. Compared to grounded ice that characterize the western Arctic shelves, the backscattered fast ice signatures in the south-eastern Laptev Sea are generally low (-17.56 ± 0.67 dB in winter). According to Eicken *et al.* [2005] the low σ^0 values can only be explained by the lack of roughness or deformation features. The melt-onset of fast ice (Figure 7c) is accompanied by an increase of reflected microwave energy. There are two mechanisms responsible for the observed increase. At relatively low water volumes (1 to 3 %) the large brine wetted snow grains in the basal layer contribute a significant volume scattering term to σ^0 .

As the water in liquid phase continues to increase, it is likely that the snow surface contributes a surface scattering term to σ^0 [Barber *et al.*, 2000].

[26] The increase in fast ice radar brightness at the end of winter is widely used to estimate the time of melt-onset. Monitoring and mapping melt parameters using active and passive microwave data provide spatial and temporal information about variations in the surface energy balance. Therefore we developed an algorithm, calculating winter σ^0 means for sample points throughout the fast ice area, and interpolating the backscatter evolution in between two image pairs by a linear function. Then a threshold value for the melt-onset is defined. The day when $\sigma_n^0 >$ threshold value is taken as the melt onset. Various detection methods and threshold settings are discussed in literature [Belchansky *et al.*, 2004; Cavalieri *et al.*, 1990; Winebrenner *et al.*, 1994].

[27] The phenomenological profile of ice located next to the river mouth (bottomfast ice) significantly differs from fast ice. A continuous increase in backscatter until end of December is related to ice thickening taking place (Figure 7d). Following Jeffries *et al.* [1996] and Eicken *et al.* [2005], the high backscatter coefficient of low salinity ice in the rivermouth during winter months is caused by tabular air inclusions (Figure 7e). Grey tones in the rivermouth zone vary between -6 dB and -12 dB. Variations can be partially explained whether the ice is frozen to the bottom or not. Light tones denote strong backscatter from ice that has water beneath it (high dielectric constant). Darker tones denote from ice that is frozen to the bottom (lower dielectric contrast at ice-water interface). The rapid decrease in sigma nought in May is presumably caused by flooding events (Figure 7f). On average, river flooding starts between end of May and beginning of June [Bareiss *et al.*, 2005]. The overflow of the nearshore ice dampens microwave scattering and speeds up fast ice melting and retreat.

[28] For mapping of coastal flooding events, an algorithm was developed, that automatically detects overflow-related decreases in σ^0 . Due to lack of time for the preparation of this thesis, the introduced algorithms for melt- and flooding-onset detection are far from finished. Inconsistencies have been found and further calibration needs to be carried out first. In addition we found the temporal coverage of our time series in spring to be insufficient for measuring geophysical and thermodynamic sea-ice states, as it does not extent far enough into July.

3.4 Polynya backscatter signatures

[29] Because of their accessibility, coastal and flaw polynyas have been studied more frequently than sensible heat polynyas³. Figure 8 presents an idealized schematic drawing of the geophysical processes taking place inside the SWNS polynya and a corresponding ASAR backscatter profile from

³ Thermally driven polynya. They appear as a result of oceanic sensible heat entering the area of polynya formation in amounts large enough to melt any pre-existing ice and prevent the growth of new ice [Morales Maqueda *et al.*, 2004].

an image taken on March 8, 2004: Prevailing southerly winds (180°) advect the ice cover away so that open water is exposed and heat is released to the air. With distance from the coast, the wave amplitude and wavelength increase and so does the backscattered radar energy (see radar profile Figure 8b). For wind speeds greater than 5 m s^{-1} , the interaction of the wave with the wind stress creates circulation within the water column. Following *Martin* [2001], “the circulation consist of rotating vortices with the rotor axes approximately parallel to the surface winds, where adjacent rotors turn in opposite directions and the rotor diameter is approximately equal to the bottom depths in well mixed waters...”. The circulation (convective mixing) and wave interaction mixes the upper water column and cools it down to freezing point so that frazil crystals⁴ are formed. Brine rejection during the formation of frazil ice increases the thickness of the convective mixing layer and eventually contributes to the development of cold saline waters.

[30] Once ice crystals reach the surface, the circulation herds them into slurries, visible as grey strikes (Langmuir strikes) in between bright water strips on the ASAR image (Figure 9). Wind pushes

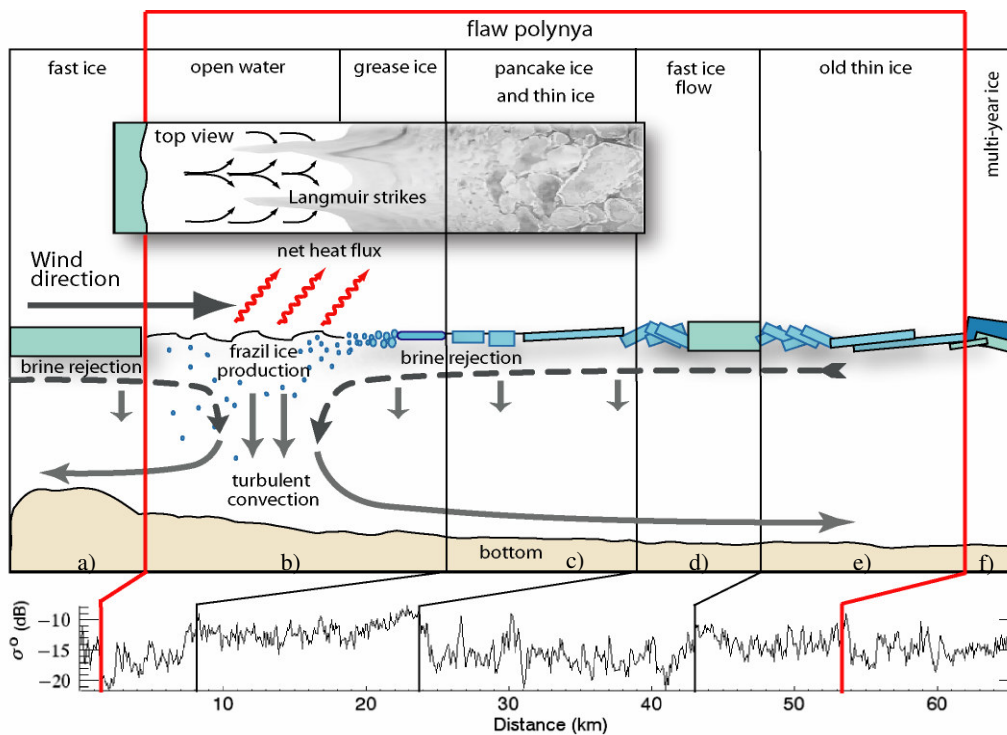


Figure 8. Schematic drawing of geophysical processes taking place inside the SWNS flaw polynya and the corresponding SAR backscatter profile from an ENVISAT WSM VV image taken on March 8, 2004. The different sections of the SAR profile are explained in the text.

⁴ Collection of loose, randomly oriented ice crystals formed below -1.8°C [Wikipedia]

the long bands of grease ice downwind, so they increase in thickness and damp out the wave amplitude and frequency. Finally, the grease ice surface freezes and pancake ice is formed through longer ocean swell and wave-induced collisions, until the thin ice piles up against the edge of the pack ice or freely floating fast ice. In section c of Figure 8, the radar profile exhibits a downwind increase in intensity provoked by increasing surface roughness. The inhomogeneous backscatter profile of section 8d represents a large ice floe that broke off earlier from the fast ice edge. Both, the downwind and upwind site of the thick floe shows pile-up and deformation signatures (high σ^0). Profile 8e belongs to an older thin ice area. Since ice thickening took place, scattering is slightly reduced compared to the newly formed thin ice of profile 8c.

[30] Under calm wind conditions (less than 5 m s^{-1}), the ice export slows down and frazil ice or thin ice is formed immediately adjacent to the coast [Martin, 2001]. The Langmuir circulation is no longer evident in the radar image. If the wind stops blowing completely, the slurries and thin ice cover freeze into a solid thin ice layer, the so called nilas ice.

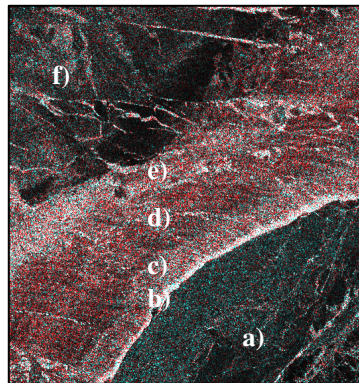


Figure 9. A ENVISAT APP colour composite of the SWNS polynya on March 25 (R: HH; G: VV; B: VV). The width of the polynya is approximately 6 km. The wind direction is 115° and the wind velocity around 7 m sec^{-1} . On the image, a) is the fast ice cover, b) shows a narrow wind roughened open water stripe, c) is the Langmuir plumes (parallel to the wind direction), d) is grease ice, e) is piled up thin ice and grease ice and f) is pack ice and freely floating fast ice.

4. Polynya evolution and ice production model

[31] Because in general, coupled ice-ocean general circulation models (OGCMs) do not have a sufficient spatial resolution to represent polynya events, special polynya models are widely used to predict how the area of a polynya will develop in time. The polynya flux models, boundary layer models or dynamic-thermodynamic sea-ice models provide more accurate information about ice

formation and associated salt rejection to parameterize the water mass transformation processes that take place within OGCMs [Morales Maqueda *et al.*, 2004]. As inputs for polynya models, oceanic and meteorological data are required. In addition, the implementation of geophysical processes such as frazil and consolidated ice drift velocity and thickness, ice pile up and rafting is crucial.

[32] In this study, the model used to reconstruct the ice flux of the SWNS polynya is based on an approach of *Haarpaintner et al.* [2001]. The model is categorized as a flux model which was first formulated by *Pease* [1987], embracing an idea of *Lebedev* [1968] that wind-generated coastal polynyas attain a certain maximum size. According to *Pease's* Steady State Model, which describes the polynya size in terms of four variables, the width is determined by a balance between ice production within the polynya and the flux of ice out of the polynya:

$$R = h_c \cdot U_{ice\ drift} / h_f, \quad (2)$$

where R is the polynya width, h_c the consolidated frazil ice accumulation thickness, $U_{ice\ drift}$ the ice export velocity away from the polynya and h_f the frazil ice growth in open water regions given in $m\ sec^{-1}$ [Drucker *et al.*, 2003].

[33] The *Haarpaintner* polynya approach, which was first applied to the Storfjorden polynya during winter 1997/1998, idealizes ice dynamics by the classification of the ice cover on pairs of ASAR images and interpolates in between using polynya widths models. The open water widths R_{OW} and the total polynya widths R_{total} are separately reconstructed. Within the open water area, frazil ice is assumed to grow at a rate determined from the surface heat budget [Cavalieri *et al.*, 1994]. Wind stress herds the frazil ice downwind until it consolidates as new ice with the thickness h_c at the offshore edge of the polynya. Surface currents are not taken into account. The continuous thin ice growth (dH) in the thin ice area is calculated based on Stefan's law, assuming an initial thin ice thickness of h_c for every polynya event. Based on the calculated ice growth dH and frazil ice growth h_f , the associated brine production is derived.

[34] The following sections explain the method used and formulates the algorithms. The results are discussed and compared to literature in section 6. For a more extensive description of the applied algorithms see *Haarpaintner et al.* [2001]. A model work flow is given in the Appendix (A1).

4.1 Modelling polynya evolution

4.1.1 Polynya segmentation

[35] To calibrate the polynya width model, polynya widths information is extracted manually from the calibrated satellite imagery. 45 WSM-, 34 APP-ENVISAT and 150 AVHRR images provide

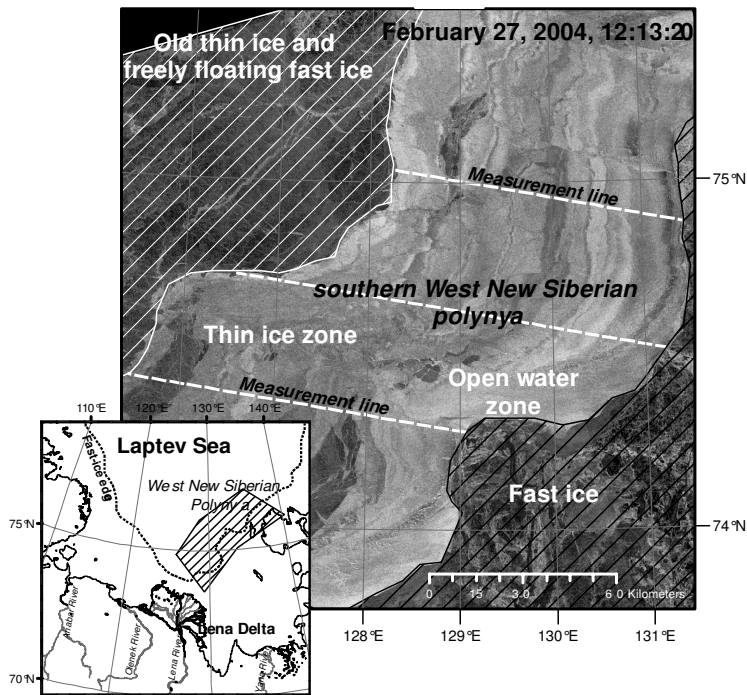


Figure 10. WSM image taken on February 18, 2004, segmented into four different features: Open water, fast ice, older thin ice and thin ice. The dashed bars represent polynya width measurement lines.

valuable information about the SWNS polynya evolution in time. Details about processing and image enhancement for visual interpretation and segmentation are given in chapter 2.1 and 2.2.

[36] In the images we consider regions of four different ice types: Open water and thin ice, defining the active polynya zone, and fast ice and old deformed thin ice or pack ice, limiting the polynya dimension. Along three lines parallel to the dominant wind direction (ϕ_0) with the strongest effect in opening of the polynya, the widths of the active zone is measured and averaged to a total single polynya width. Figure 10 shows a WSM ASAR image taken on February 18, 2004, classifying the SWNS polynya into thin ice, open water, old thin ice and fast ice. The polynya widths measurement lines are indicated by white dashed bars.

[37] The challenge is to reliably identify the active polynya extent consisting of thin ice and open water. The fast ice region, limiting the southern extent of the SWNS polynya, is assumed to be constant, since it is not moving. The downwind polynya extent is restrained by pack ice or older deformed thin ice coverage. The homogeneous backscatter of old thin ice, fast ice and pack ice shows only moderate or no changes in sequential images.

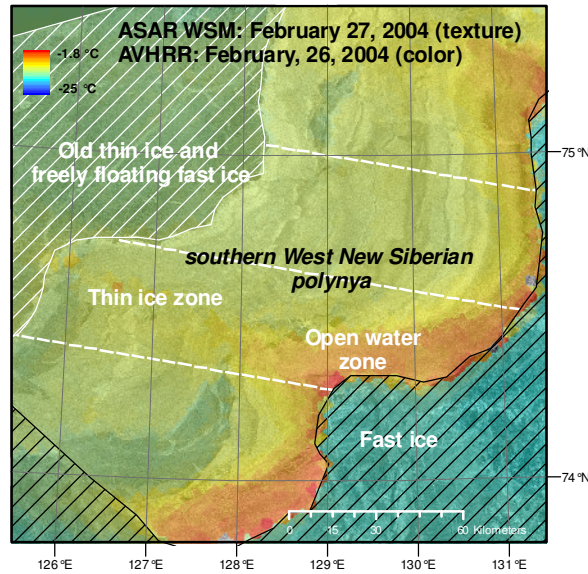


Figure 11. AVHRR and WSM ASAR composite

[38] The backscatter coefficient of the polynya itself is quite variable with strong dynamics in the time-series. The appearance of open water in the ENVISAT scenes is a function of incident angle, wind velocity and open water width. The generated wind-wave field strengthens the backscattered microwave energy as the wave amplitude and wavelength increase away from the coast. Under windy conditions (wind speed greater than about $5\text{-}10\text{ m s}^{-1}$) [Martin, 2001], the presence of Langmuir circulation parallel to the wind direction supports the identification of open water in ASAR imagery. A low sea state (wind speed less than 5 m s^{-1}) results in development of nilas ice. Similar to open water at calm wind conditions, this very thin elastic crust of ice has a low backscatter coefficient. Discrimination of ice/water is therefore complicated and not always possible with low resolution VV-polarized WSM images alone.

[39] To more accurately depict the location of the ice edge, ice concentration and ice stage of development we use ASAR/AVHRR composites from near-concurrent images. Due to a lack of time for preparing the thesis, the absolute Ice Surface Temperature (IST) could not be derived from the atmospherically corrected AVHRR images. However, the combination of the radar texture with the AVHRR information of channel 5 reveals sufficient additional indices for open water identification. Figure 11 shows an atmospherically corrected AVHRR image (channel 5) taken on February 26, pansharpened with a WSM scene, taken approximately one day later. The spatial distribution of bright AVHRR pixels (red in the composite) coincide with locations of Langmuir stripes in the radar image. We therefore expect bright pixels to be equal to the freezing point of open water (-1.8 °C) and dark ones to be close to the recorded air temperatures appearance of fast ice and pack ice: The dark first

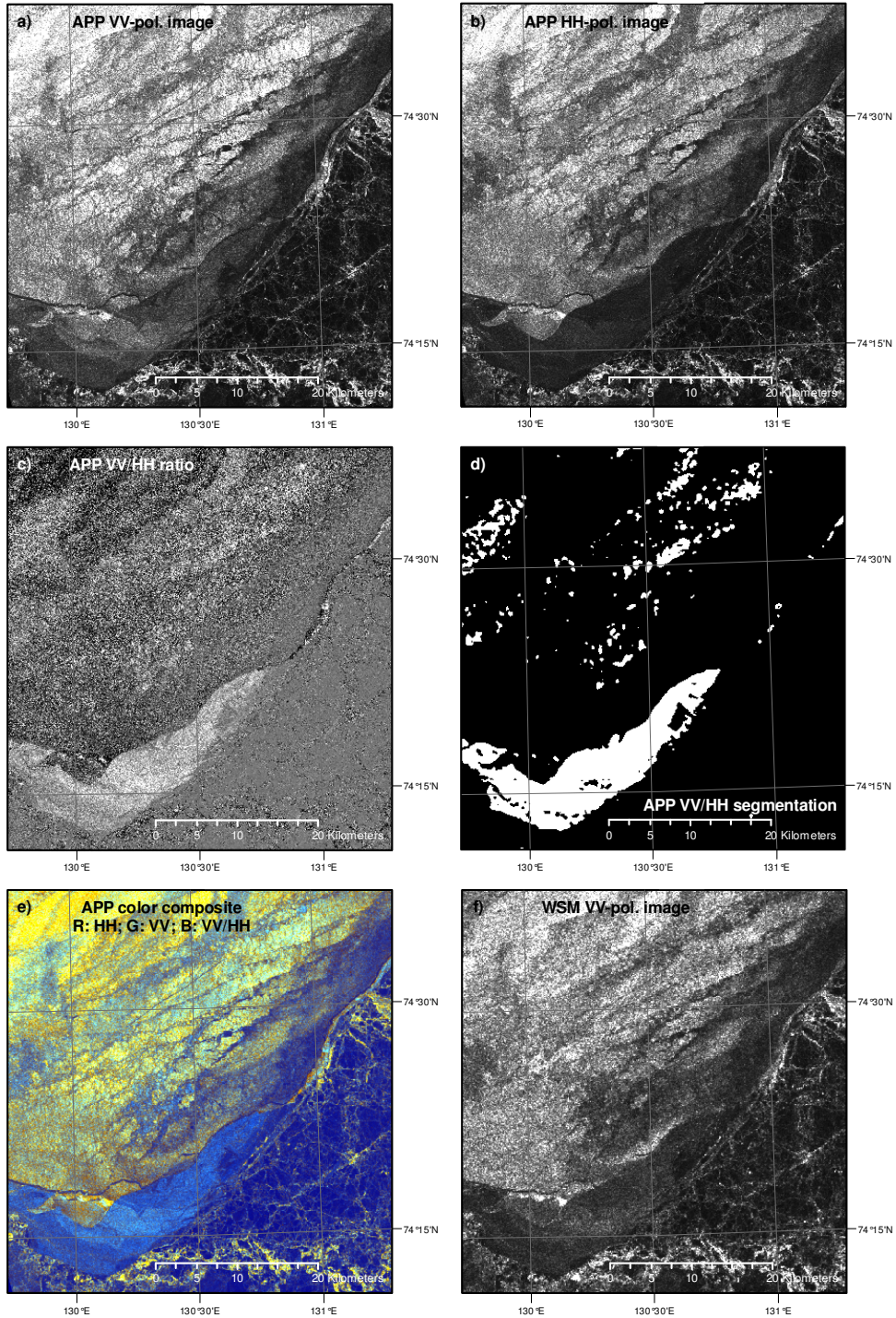


Figure 12. Automatic polynya classification of an APP image taken on March 4, 2004: The co-polarization ratio c) of a VV- and HH-polarized APP ENVISAT image a) and b) is segmented using a simple threshold based classifier d). A colour composite of HH, VV and VV/HH-polarization is given in e). A WSM scene (March 5, 2004) covering the same region with lower spatial resolution is given in f).

year ice in the south is nerved by bright bands indicating ice deformation processes. The rough surface and higher volume scattering of the pack ice in the north results in a brighter and more inhomogeneous signature. Using only low resolution WSM imagery (f), the area in between the fast- and multi year ice is difficult to define. However, the co-polarization ratio enables a more exact differentiation. Since the ratio of VV to HH backscatter is larger than 1 for open water and nilas ice, but close to 1 for fast ice and pack ice, thicker ice is seen to be much darker on the co-polarization ratio image (c), independent of incidence angle or wind condition. The sharp contrast between fast ice/pack ice and thin ice/open water in co-polarization ratios certainly possess great potential for automatic polynya segmentation. For demonstration, we applied a simple threshold based classifier to the filtered HH/VV image (d).

[41] Despite of the amount of satellite data and segmentation techniques used, on several images it is still very difficult to discriminate the active polynya zone from the adjacent ice. These images have been excluded from the model calibration procedure (see section 6.1).

4.1.2 Total polynya width reconstruction

[42] Following *Haarpaintner et al.* [2001], the first model approach is to reconstruct and interpolate the evolution of the polynya in size, estimated subjectively from the ASAR imagery. According to *Pease* [1987], opening and closing of latent heat polynyas in time can be described in terms of wind direction, wind velocity and ice export. Thus, *Haarpaintner et al.* developed a simple wind-driven ice drift algorithm:

$$R_{total} = R_{total(n-1)} + A(\varphi_n - \varphi_o) \cdot B_I \cdot U \cdot \cos(\varphi_n - \varphi_o) \cdot \Delta t, \quad (3)$$

where R_{total} is the polynya width at time n (sum of thin ice width and open water width), U is the wind velocity in m sec^{-1} , in our case recorded at the Dunai weather station, Δt the time interval between two meteorological measurements and B_I the thin ice drift velocity in percent of wind speed. $A(\varphi_n - \varphi_o)$ is the opening and closing factor, where φ_n is the recorded wind direction and φ_o is the dominant wind direction with strongest effect on the opening of the polynya. The constant $A(\varphi_n - \varphi_o)$ factor, which differs for opening and closing, is defined by:

$$\begin{aligned} \text{if } -90^\circ < \varphi_n - \varphi_o < 90^\circ &\Rightarrow \text{opening} \\ \text{if } 90^\circ < \varphi_n - \varphi_o < 270^\circ &\Rightarrow \text{closing,} \end{aligned} \quad (3.1)$$

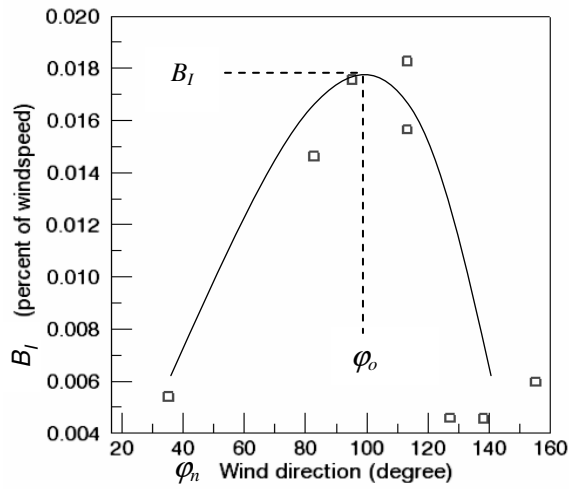


Figure 13. Ice flows inside the polynya are tracked on 8 WSM image pairs. The Figure plots the observed B_I values over the recorded wind direction between image dates.

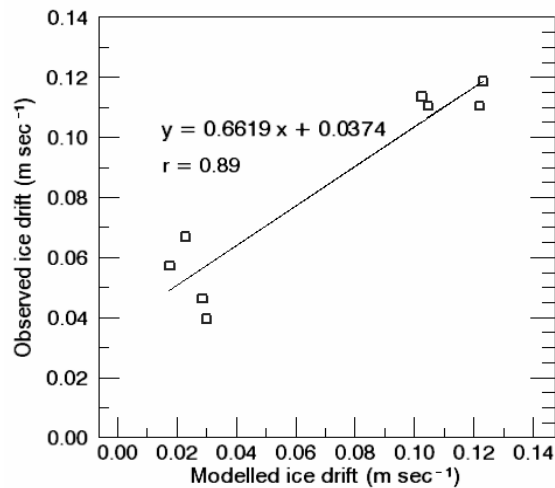


Figure 14. Model calibration: Observed over modelled ice drift rates ($U_{ice\ drift}$)

The meteorological data recorded at the Dunai station reveals two main wind directions in the south-eastern Laptev Sea: The wind direction plot in Figure 2 peaks at 180° (southerly winds) in early winter between October and end of January and at 90° (easterly winds) after February [Haas *et al.*, 2004a]. Consequently, we found that southern winds open the polynya until early February, while in second half of winter eastern winds govern the polynya form. Opposite wind directions result in a close up. Therefore, we model the widths evolution under the two wind regimes separately, using different $A(\varphi_n - \varphi_o)$ constants, one for the first and one for the second half of winter.

[43] The ice drift velocity of thin ice B_I is typically taken as 2% (0.02) of the wind velocity [Nansen, 1906]. To obtain more precise information about B_I in the SWNS polynya, ice floes inside the thin ice regions are tracked on 8 ASAR image pairs between February 05, and May 26, with approximately 10 hour time difference. Figure 13 plots the 8 measured B_I values over the recorded wind direction between two image dates. The thin ice drift velocity B_I in percent of U peaks with 1.8 % at a wind direction of 100° . Based on

$$U_{ice\ drift} = U \cdot B_I \cdot \cos(\varphi_n - \varphi_o) \cdot \Delta t \cdot A(\varphi_n - \varphi_o), \quad (3.2)$$

a sensitivity study of $A(\varphi_n - \varphi_o)$ and φ_o is performed, taking B_I as 1.8 % (0.018). Figure 14 presents the observed and modelled $U_{ice\ drift}$. For the second winter period, dominated by eastern winds, the highest correlation of 0.89 is found, if setting the dominant wind direction (φ_o) to 100° and $A(\varphi_n - \varphi_o)$ to 0.8 (opening) and 13 (closing). A systematic validation of the early winter period through equation 3.2 is not possible, since only three ASAR observations between January 07, and February 05, are available. For further fine-tuning, the results of the sensitivity study for the second winter period are used as inputs for equation 3. The model gives best fit between observed and calculated R_{total} at $\varphi_o = 110^\circ$, $A(\varphi_n - \varphi_o) = 0.72$ (opening) and 15 (closing) (Figure 15). The early winter period, dominated by southerly winds, is roughly calibrated using the three ASAR observations by setting φ_o to 180° and $A(\varphi_n - \varphi_o)$ to 0.72 (opening) and 14 (closing), respectively. Table 1 summarizes the parameterized driving forces for opening and closing events under the two wind regimes.

Winter period	φ_o	$A(\varphi_n - \varphi_o)$	$A(\varphi_n - \varphi_o)$	B_I
		opening	closing	
Oct. - Jan.	180°	0.72	14	0.018
Feb. - June	110°	0.72	15	0.018

Table 1. Total width model inputs (equation 3.2) for the SWNS polynya

It was found that most of the time closing occurs much faster than opening. This can be explained by the frazil ice that accumulates at the lee-site of the polynya under a north-western wind regime, which consolidates and closes the polynya by thickening and compression. If temperatures rise about -1.8°C (freezing point of sea water), the net heat flux of open water becomes negative, frazil ice production stops and polynya closing events are slowed down. Therefore, the model is limited to air temperatures below -1.8°C .

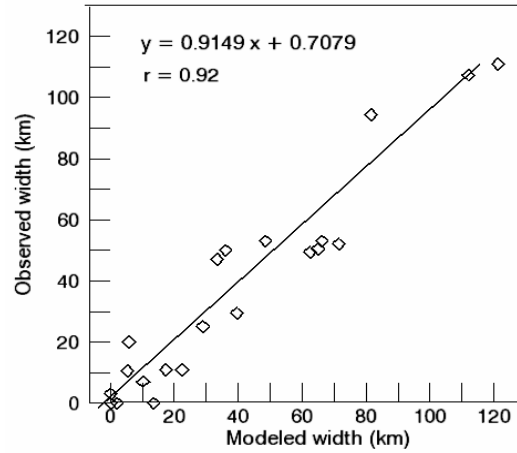


Figure 15. Model calibration: Observed (ASAR) over modelled polynya width ($r = 0.92$), setting φ_o to 110° , $A(\varphi_n - \varphi_o)$ to 0.72 (opening) and 15 (closing) and B_I to 1.8 %

4.1.3 Open water width reconstruction

[44] To reconstruct the evolution of open water, three different open water models are applied and evaluated.

[45] The first approach (Equation 4) takes the effect of high frazil ice production rates (see section 4.2.2) during periods of low air temperatures and high wind speeds on open water dynamics into account. Following *Haarpaintner et al.* [2001], the open water fraction of the total polynya width can be expressed as:

$$R_{OW} = R_{OW(n-1)} \cdot \left(1 - \frac{\Delta h_f}{h_c} \right) + b_I \cdot U \cdot \cos(\varphi_n - \varphi_o) \cdot \Delta t, \quad (4)$$

where R_{OW} is the open water width at time n , b_I is the frazil ice drift velocity in percent of the wind speed (1 % higher than B_I), h_c is the consolidated frazil ice thickness and Δh_f is the amount of frazil ice produced between n and $n-1$ (see section 4.2.2). The polynya fraction covered with open water is given by $(1 - h_c / \Delta h_f)$. Thus, high frazil ice production rates (Δh_f) close, while low ice production rates enlarge the open water area. The consolidated frazil ice thickness h_c is chosen during model calibration such that the modelled open water widths match the satellite observations. In literature, different values to account for the accumulation thickness h_c are used. *Pease* [1987] assume that h_c is between 5 and 30 cm, *Haarpaintner et al.* [2001] assume h_c to be 20 cm, and *Windsor et al.* [2000] assume that the accumulation thickness is a linear function of the 10-m wind speed. *Morales Maqueda et al.* [2000] choose h_c as 10 cm, and *Biggs et al.* [2000] set h_c to 48 cm [*Drucker et al.*, 2003]. Our

modelled open water widths fit the satellite observations best, if h_c is constant around 11 cm. Figure 16a shows the regression plot between modelled and observed open water widths for a constant h_c ($r = 0.635$).

[46] Following Pease [1987], the velocity of frazil ice in percent of wind speed b_I is taken to be 1% (0.01) higher than B_I , since the drift resistance in open water zones is less than in thin ice zones. Therefore, frazil ice can be expected to accumulate faster on the thin ice lee-side under windy conditions. This effect is simulated, if h_c is supposed to be a function of wind-velocity. The implementation of a logarithmic h_c that increase from 5cm to 15cm as the wind velocity increases from 1 to 8 m sec⁻¹

$$h_c = 0.05 \cdot \log(U) + 0.04, \quad (4.1)$$

results in a slightly higher correlation coefficient r of 0.643 (Figure 16b).

[47] In the third R_{OW} approach, we neglect the $\Delta h_f / h_c$ ratio of equation 4. Comparing different polynya stages from ASAR imagery with meteorological data shows that equation 4 underestimates the velocity of freeze-up events under periods of weak and very cold winds. Since the frazil ice production rate Δh_c considered in equation 4 is empirically included in the $A(\varphi_n - \varphi_o)$ factor, we implement freeze-up events in equation 3 by:

$$\begin{aligned} &\text{if } U > 3 \text{ m sec}^{-1}: \\ &R_{OW} = R_{OW(n-1)} + A(\varphi_n - \varphi_o) \cdot b_I \cdot U \cdot \cos(\varphi_n - \varphi_o) \Delta t, \\ &\text{if } U < 3 \text{ m sec}^{-1} \text{ for } \Delta t > 48 \text{ hours:} \\ &R_{OW} = 0, \end{aligned} \quad (5)$$

The $A(\varphi_n - \varphi_o)$ values are taken from equation 3. The freeze-up threshold ($U < 3 \text{ m sec}^{-1}$ for $\Delta t > 48 \text{ hours}$) is chosen during model calibration, such that the open water widths extracted from ASAR imagery match the modelled widths. The obtained correlation coefficient r is 0.7. Before ice can drift northward and re-open the polynya after freeze-up events, some energy is needed to break-up the newly formed thin ice layer from the fast ice edge. The delay of break-up events varies with the drag forces acting on the ice cover. We expect it to be a function of wind velocity, wind direction and sea-ice roughness (deformation). However, due to a lack of ASAR observations, this process could not be reliably implemented so far. Figure 16c presents the regression plot of the third open water modelling approach. The effect of using different open water models (constant h_c , logarithmic h_c and freeze-up simulation) on the total ice and salt flux is discussed in section 5.1.

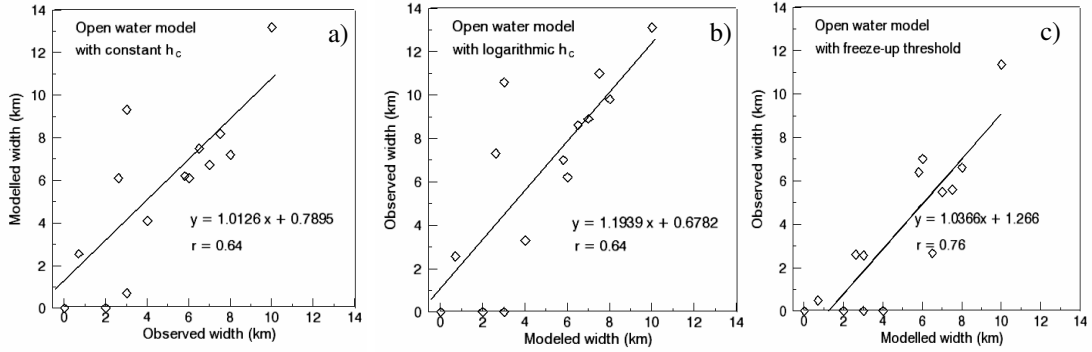


Figure 16. Regression plots of observed (ASAR) and calculated (model) open water widths. a) gives the model performance using a constant h_c value, b) using a logarithmic h_c value and c) using a freeze-up threshold.

4.1.4 Polynya area

[48] We apply equation 3 through 5 to interpolate the total polynya widths and the open water fractions. The width of the thin ice cover is calculated by:

$$R_{TI} = R_{total} - R_{OW},$$

AVHRR imagery and AMSR-E sea-ice concentration data show that the SWNS polynya is relatively constant in length during winter 2003/2004. For calculation of open water (A_{OW}) and thin ice area (A_{TI}), the thin ice and open water widths is multiplied with a 195 km length l (Figure 17):

$$A_{total} = R_{total} \cdot l = A_{OW} + A_{TI} = (R_{OW} \cdot l) + (R_{TI} \cdot l), \quad (6)$$

4.2 Modelling ice growth

4.2.1 Open water heat budget

[49] Over open water or thin ice (<10 cm thick, so that thermal inertia can be neglected) the surface heat balance can be decomposed as:

$$Q_T + Q_L - Q_B - Q_S = Q_{net}, \quad (7)$$

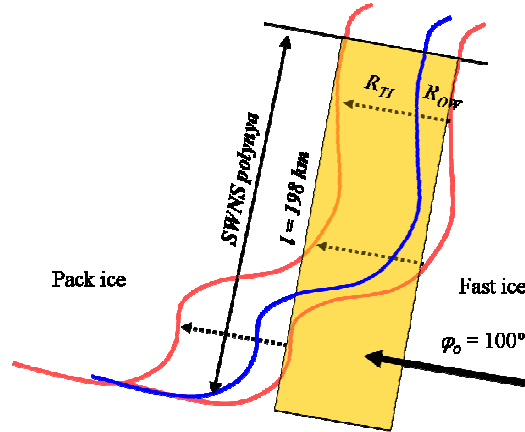


Figure 17. Geometry of the SWNS polynya. R_{TI} and R_{OW} are the thin ice and open water width, respectively. l defines the polynya length and φ_o is to the dominant wind direction. The area (orange square) is the product of polynya width and polynya length.

where Q_T is the upward turbulent heat flux, Q_L is the upward component of the longwave radiation emitted by the sea, Q_B is the downward atmospheric longwave radiation absorbed at the ocean surface and Q_S is the shortwave solar radiation. If Q_{net} is positive, the water column gains heat. The terms given in equation 7 are described below:

[50] The turbulent heat flux is expressed as:

$$Q_T = \rho_a C c_p U(T_a - T_s), \quad (7.1)$$

with air density ρ_a of 1.3 kg m^{-3} , a heat transfer coefficient C of 2.0×10^{-3} and the specific heat of air at constant pressure c_p of $1004 \text{ J deg}^{-1} \text{ kg}^{-1}$. U is the wind speed and T_a is the air temperature observed at the nearby weather station. T_s is the sea surface temperature. The ocean surface in the polynya is assumed to be at the freezing point of sea water during the winter period ($T_s = -1.8 \text{ }^\circ\text{C}$). Turbulent heat losses is the single most important component of the surface heat balance over winter polynyas, contributing up to 75% of the total heat loss [Winsor et al., 2000].

[51] The emitted upward component of the longwave radiation is expressed by the Stefan-Boltzmann law:

$$Q_L = \varepsilon_s \sigma T_s^4, \quad (7.2)$$

where σ is the Stefan-Boltzmann constant and ε_s the water surface emissivity (0.98). Because the sea surface temperature T_s is fixed at -1.8°C , the upward longwave radiation Q_{lwo} is constant around 298 W m^{-2} .

[52] The downward atmospheric longwave radiation Q_{lwa} is expressed as:

$$Q_B = \varepsilon_s (\varepsilon_a \sigma T_a^4), \quad (7.3)$$

where $\varepsilon_a = 0.7829 (1 + 0.2232 \cdot CL^{2.75})$ and CL is the cloud cover. Since we do not have cloud observations over the Lena Delta between January and June 2004, CL is assumed to be constant at 0.8. Following *Maykut* [1986], for air temperatures within the range from -20°C to 0°C , the difference in Q_B between clear conditions and overcast is only 40 Wm^{-2} . The sensitivity study in section 5.1 evaluates the effect of varying cloud coverage (± 0.2) on the salt and ice flux calculation.

[53] The net shortwave radiation is an important component of the surface heat budget in the summer period when the sun is high enough above the horizon, but can be neglected during winter. Following *Markus et al.* [1998], the incoming solar radiation is

$$Q_s = \frac{S_0 \cdot \cos^2 z}{1.085 \cdot \cos z + (2.7 + \cos z) v_p \cdot 10^{-3} + 0.1}, \quad (7.4)$$

where S_0 is the solar constant (1353 W m^{-2}), v_p is the vapour pressure and z is the sun zenith angle expressed by:

$$\cos z = (\sin \phi \cdot \sin \iota) + (\cos \phi \cdot \cos \tau \cdot \cos \iota), \quad (7.5)$$

with ϕ = latitude and τ = solar hour angle. v_p is calculated by:

$$v_p = rH \cdot v_{sat} \quad \text{with } v_{sat} = 6.11 \cdot 10^{\alpha T_a / (\beta + T_a)}, \quad (7.6)$$

where rH is the relative humidity (fixed to 0.8), $\alpha = 7.5$ and $\beta = 237.3$.

[54] For a fuller description of net shortwave radiation calculation see *Markus et al.*, [1998] and *Haarpaintner et al.* [2001]. The single components of equation 7 are presented in Figure 18.

4.2.2 Frazil ice accumulation

[55] After applying equation 7 through 7.6 to derive Q_{net} , the frazil ice production in the water column is calculated by:

$$\Delta h_f = \frac{Q_{net}}{\rho_f \cdot L_s} \cdot \Delta t, \quad (8)$$

where ρ_f is the frazil ice density of 950 kg m^{-3} and L_s is the latent heat of fusion for sea-ice:

$$L_s = 4.187 \cdot \left(79.68 - 0.505 \cdot T_s - 27.3 \cdot S_{ice} + 43115 \cdot \frac{S_{ice}}{T_s} + 0.8 \cdot S_{ice} \cdot T_s - 0.009 \cdot T_s \right), \quad (8.1)$$

L_s varies with the water (S_{water}) and ice salinity (S_{ice}). Following *Martin et al.* [1981], the salinity of ice is expressed as:

$$S_{ice} = 0.31 \cdot S_{water}, \quad (8.2)$$

Based on hydrological data from 1979 to 1999 the average water salinity of the upper water layer in the SWNS polynya is assumed to be 28 psu [*Dmitrenko et al.*, 2005]. This corresponds to $S_{ice} = 8.7$ psu and $L_s = 252 \text{ kJ kg}^{-1}$.

4.2.3 Thin ice growth

[56] A review of different mathematical treatments of simple sea-ice growth models is given in *Eicken* [2004]. To estimate the thickening of the thin ice layer we applied Stefan's law:

$$H^2 + \left[\frac{2k_i}{k_s} h_{s+} \frac{2k_i}{C_t} \right] \cdot H = \frac{2k_i}{\rho_i L} \theta \Leftrightarrow$$

$$dH = \frac{2k_i}{\rho_i L \cdot \left[2H + \left(\frac{2k_i}{k_s} h_{s+} \frac{2k_i}{C_t} \right) \right]} d\theta, \quad (9)$$

where H is the ice thickness given in cm, h_s is the snow cover thickness, k_s describes the thermal conductivity of snow ($= 0.31 \text{ W m}^{-1} \text{ K}^{-1}$), k_i the thermal conductivity of ice ($= 2.03 \text{ W m}^{-1} \text{ K}^{-1}$), C_t is the net surface heat exchange ($= 0.24 \text{ W m}^{-1} \text{ K}^{-1}$), ρ_i is the ice density ($= 920 \text{ kg m}^{-3}$), and L is the

latent heat of fusion ($\rho_i L = 272 \text{ J cm}^{-3}$ for 10% brine volume). θ is the cumulative number of freezing degree days (*FDD*), defined by:

$$FDD_n = \sum_{i=1}^n (T_s - T_a), \quad (9.1)$$

Where n is the number of consecutive days, T_s is the sea surface temperature at freezing point, and T_a is the averaged daily air temperature recorded at the Dunai weather station.

Evaluating equation 8 with the inputs given above, we obtain following general expression for H (in cm):

$$H^2 + [13.1h_s + 16.8] \cdot H = 12.9\theta \Leftrightarrow dH = \frac{12.9}{2H + 13.1h_s + 16.8} d\theta, \quad (9.2)$$

Since it is new ice, we neglect the snow layer, reducing the equation to [*Haarpaintner et al.*, 2001]:

$$H^2 + 16.8H = 12.9\theta \Leftrightarrow dH = \frac{12.9}{2H + 16.8} d\theta, \quad (9.3)$$

Following *Haarpaintner et al.* [2001], we assume the initial ice thickness for every polynya event to be equal to the frazil ice accumulation depth h_c . However, the continuous opening and closing of the polynya leads to compression and dispersion of the thin ice thickness. The conservation of mass inside the polynya is considered by:

$$H_n = \frac{(A_{TI(n-1)} \cdot H_{(n-1)}) + (A_{OW(n-1)} \cdot \Delta h_f)}{A_{TI n}}, \quad (9.4)$$

4.3 Salt fluxes

[57] To study the impact of the SWNS polynya on saline shelf water formation in the Arctic Ocean, we roughly determine the amount of salt released based on the modelled ice production. For a salt flux computation the initial water salinity needs to be known. *Dmitrenko et al.* [2005] analyzed the impact of latent heat polynyas in the Laptev Sea on surface salinity, along with variable river runoff and atmospheric forcing. Hydrological data from 1979 to 1999 provide long-term average salinity data and

their variance for the Laptev Sea. *Dmitrenko et al.* [2005] found intensive river runoff and ice melting in summer to be responsible for relatively low water salinity throughout the year. Based on their long-term observations, we consider the average water salinity to be around 28 psu (practical salinity units) during winter 2003/2004. Due to intensive ice production and the lack of river runoff (10 % in winter months), the salinity of the surface layer is expected to increase towards spring. *Dmitrenko et al.*, [2005] measured the seasonal surface salinity to vary by 3.5 to 4.2 psu throughout the winter season. Unfortunately we do not have precise information about the salinity variance. Therefore we assume the salt concentration to be constant between January and June. Following *Haarpaintner et al.* [2001], a spontaneous salt rejection of 69 % during ice production is realistic. Additionally, 10-15% of the initial salinity is released during continuous ice growth, aging and cooling, though gravity drainage and flushing during melting [*Haarpaintner et al.*, 2001].

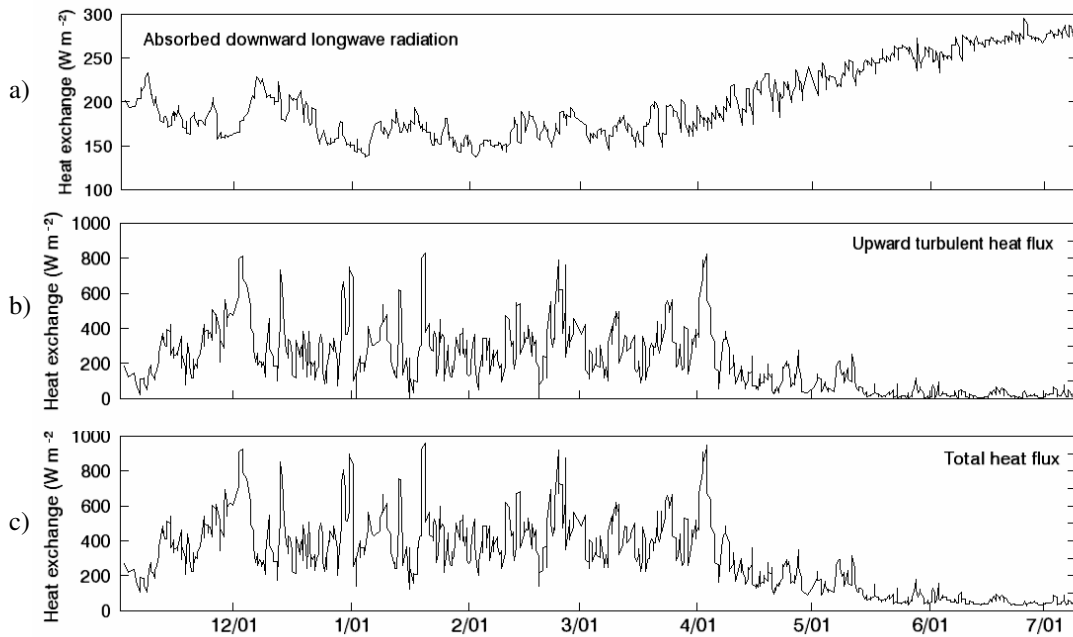


Figure 18. Heat exchange components over time: a) the absorbed downward longwave radiation at the ocean surface Q_B , b) the turbulent heat flux Q_T and c) the total net flux Q_{net} . The upward longwave radiation Q_L is constant around 298 W m^{-2} . During winter period, the net shortwave radiation Q_S is close to 0 W m^{-2} .

5. Polynya model results

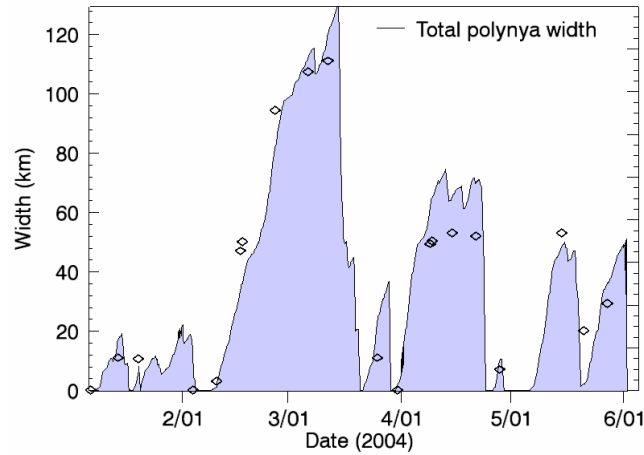


Figure 19. Modelled total polynya width (line) presented together with the ENVISAT ASAR width observations (dots) over time. The total width is the sum of thin ice and open water width.

[58] In the following chapter we show results of the polynya model described in section 4. Therefore, we applied equation 3 through 3.2 to reconstruct the polynya widths evolution in time. Since the open water model based on equation 4 with a constant h_c of 11 cm is least sensitive to disparities in the meteorological dataset and empirical coefficients (section 5.1), it is used for open water computation in the following chapter. The derived widths are multiplied with the polynya length to obtain the thin ice area and open water area. The total ice production is the sum of ice produced in the thin ice region based on Stefan's law, (equation 9 through 9.4) and the frazil ice production in the open water column (equation 7 through 8.2).

[58] Figure 19 presents the modelled polynya total width evolution and width measurements obtained from the ENVISAT ASAR imagery. The correlation coefficient r between observed and modelled widths is 0.92 with a mean deviation of 9.1 km (Figure 15). The average polynya width between January 07, and June 03, is 36 km. From February on, the SWNS polynya grows constantly until its maximum extension of around 129 km is reached on March 09, 2004. Further extensive openings occur in April and May. The sharp drop in polynya width from 20 km to 0 km on February 05, is an artificial model effect and coincident with the change from southern to eastern wind regime in the model (use of different $A(\varphi_n - \varphi_o)$ and φ_n inputs; section 4.1.2). Unfortunately, the lack of interpretable satellite data at the end of January does not allow an accurate model calibration. The overall good correlation coefficient of the model approach indicates that the meteorological data from Dunai Station is feasible for the SWNS polynya and that the model is well tuned and applicable.

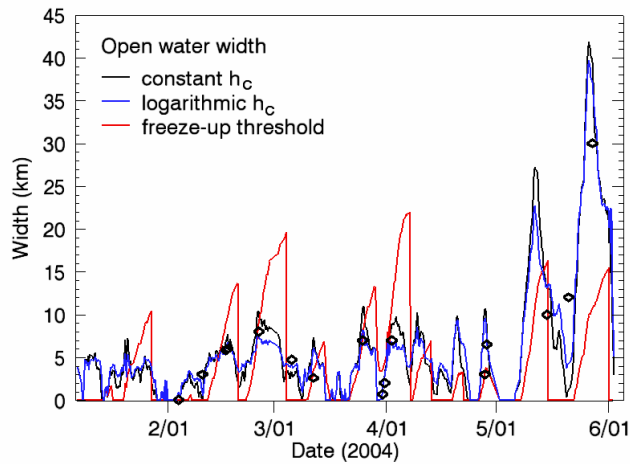


Figure 20. Modelled open water width presented together with ENVISAT ASAR WSM and APP width measurements over time. The black and blue line shows the evolution of the two h_c based open water models; the red line presents the modelled width based on equation 5.

[59] Three slightly different open water models are applied to reconstruct the evolution of open water. Equation 4 takes the frazil ice production into account with different inputs for h_c , while equation 5, neglecting the $\Delta h_f / h_c$ ratio, contains the $A(\varphi_n - \varphi_o)$ constant of equation 3 and simulates freeze-up events under calm wind conditions. Figure 20 presents the evolution of the open water fraction between January 7 and June 4, 2004 for all three approaches. The use of a constant h_c (11 cm) results in an average open water fraction of 34 % and a correlation coefficient of 0.635 (Figure 16a). Assuming h_c to be a logarithmic function of the wind-velocity, that increases from 5cm to 15cm as the wind velocity increases from 1 to 8 m sec⁻¹, results in an average fraction of 35 % and $r = 0.643$ (Figure 16b). The red line in Figure 20 represents the output of equation 5. During periods of calm wind conditions, the open water area is automatically set to zero, giving the curve a saw-blade like shape. However, we expect the high open water peaks to be overestimated, although the obtained correlation coefficient between predicted and observed widths is the highest ($r = 0.76$). Probably, ASAR measurements of the open water width are undersampled, interfering model validation.

[60] Both, the evolution of the thin ice area and open water area (with constant h_c) are plotted in Figure 21. Since the development of thin ice requires frazil ice formation first, a slight delay in thin ice growth after freeze-up events is visible in the graph. Towards end of the winter, the frazil ice productivity decreases (Figure 23), causing the delay to increase. Plotting the delay (in days) over frazil ice production, averaged between the onset of the break-up event and the onset of thin ice growth in the model, gives a correlation coefficient of 0.88 (Figure 22). We expect r to be a valuable parameter for model fine-tuning or a measure for model accuracy. However, to examine this coherence more closely, field measurements need to be carried out first.

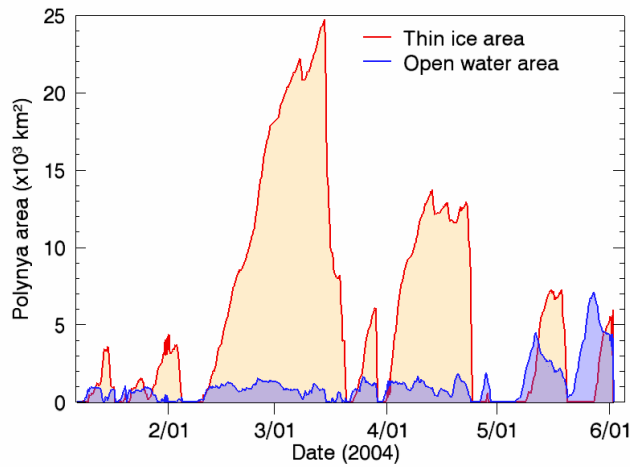


Figure 21. Modelled thin ice and open water area in the SWNS polynya.

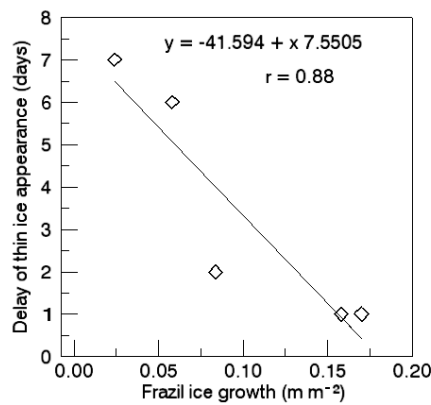


Figure 22. Delay in onset of thin ice growth (in days) over frazil ice productivity in m m^{-2} , averaged between the onset of break-up events and first thin ice formation

[61] The daily ice production in m m^{-2} for frazil ice and thin ice between January 7, and June 4, is given in Figure 23 and is a measure for the potential productivity. Daily thin ice production remains around $0.05 \text{ m m}^{-2} \text{ d}^{-1}$ between February and March. The rate of frazil ice formation follows the oscillation of the net heat flux with a peak at 0.36 m m^{-2} in early April. The increase in air temperatures in late winter lowers frazil ice and thin ice production. The average productivity of thin ice and frazil ice is 0.13 m m^{-2} and 0.04 m m^{-2} , respectively.

[62] The daily absolute ice production in km^3 in winter 2004 is shown in Figure 24. The 24h growth curve is the product of the thin ice area with thin ice production and the open water area with frazil ice production, respectively. The daily thin ice growth decreases towards June, while the ice volume produced in open water areas remains more constant, owing to an increasing open water area.

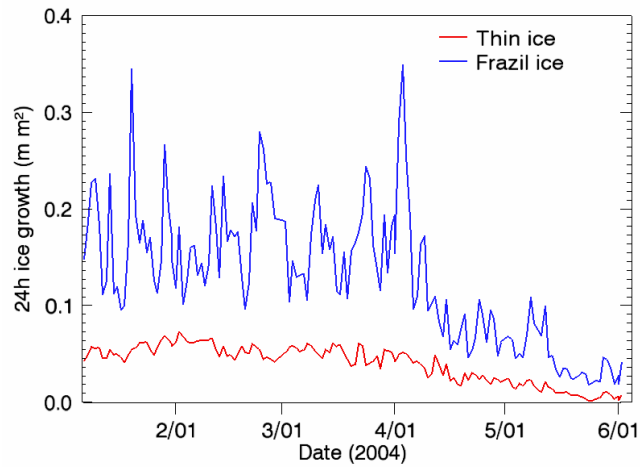


Figure 23. Daily ice production in m^2 for frazil ice (blue line) and thin ice (red line) between January 7, and June 4, 2004.

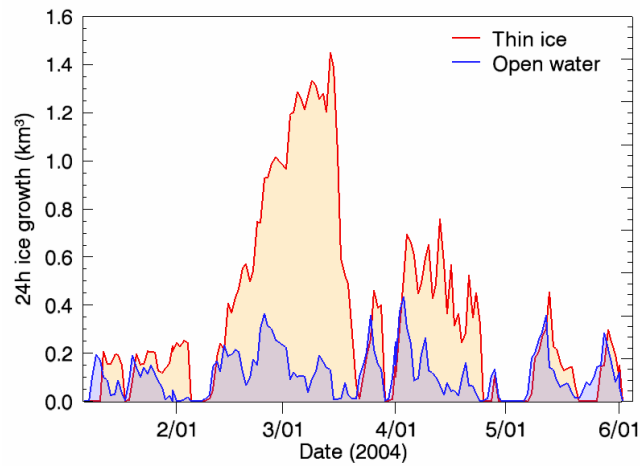


Figure 24. Daily ice production in km^3 for open water area (blue line) and thin ice area (red line) between January 7, and June 4, 2004.

[63] Figure 25 visualizes the accumulated thin ice and the accumulated frazil ice production in time. A total ice volume of 51 km^3 in thin ice and 15 km^3 in open water area is generated between January 7, and June 4. This corresponds to an ice production of 9.6 m^2 in the SWNS polynya.

[64] The daily and accumulated salt rejection from both, ice formation and aging processes, is presented in Figure 26. A total of 1506 Mt of salt is released until June 4, 2004, with a daily average rejection of 10.5 Mt .

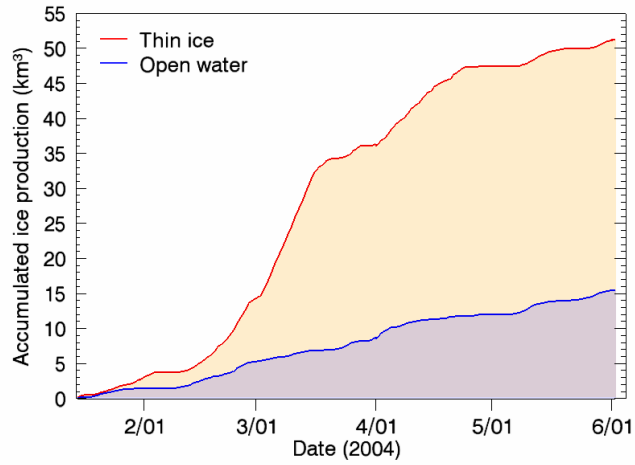


Figure 25. Accumulated ice production in km³ in open water regions (blue line) and thin ice areas (red line) between January 7, and June 4, 2004.

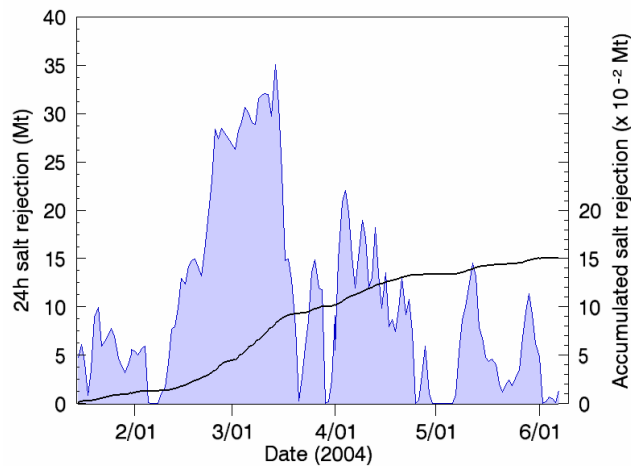


Figure 26. Accumulated salt rejection (solid black line) and daily salt rejection (blue line) of the SWNS polynya in Mt between January 7, and June 4, 2004.

5.1 Sensitivity study

[65] The high correlation coefficient of 0.92 between modelled and observed total polynya widths implies that the meteorological dataset recorded at the Dunai Station is representative for the SWNS polynya. However, the remoteness of the weather station (150 km from the polynya centre point) might result in discrepancies. Therefore, the effect of disparities between the recorded and predominant meteorological conditions is tested below. The sensitivity of the modelled sea-ice

Parameter	Variation	Model value	PEASE model with $\log. h_c$ (Equation 4)		PEASE model with constant h_c (Equation 4)		Freeze-up threshold model (Equation 5)		Average (column 1-3)	
			Ice volume (%)	Salt release (%)	Ice volume (%)	Salt release (%)	Ice volume (%)	Salt release (%)	Ice volume (%)	Salt release (%)
φ_0	$\pm 10^\circ$	$180^\circ/110_{(1)}$	± 5.5	± 5.5	± 4.7	± 4.7	± 3.8	± 3.8	± 4.7	± 4.7
b_i	$\pm 0.5 \%$	2.8 %	± 8.3	± 8.2	± 9.7	± 8.2	± 18.3	± 6.3	± 12.1	± 7.6
B_i	$\pm 0.5 \%$	1.8 %	± 18.0	± 17.8	± 19.9	± 18.2	± 31.1	± 20.2	± 23.0	± 18.7
h_c	± 4 cm	11 cm	± 12.6	± 12.4	± 12.2	± 12.2				
T_{Dunai} to T_{WNS}	$\pm 2^\circ\text{C}$	-	± 6.6	± 6.5	± 6.2	± 6.2	± 8.9	± 8.8	± 7.2	± 7.2
U_{Dunai} to U_{WNS}	± 0.5 m sec ⁻¹	-	± 5.8	± 10.7	± 4.9	± 9.3	± 10.1	± 16.7	± 6.9	± 12.2
Bulk transfer coefficient	$\pm 0.5 \times 10^{-3}$	2.0×10^{-3}	± 2.3	± 2.3	± 1.7	± 1.7	± 6.1	± 6.0	± 3.4	± 3.4
Cloud cover	$\pm 0,2$	0,8	± 1.0	± 1.0	± 1.1	± 1.1	± 1.3	± 1.3	± 1.1	± 1.1
Relative humidity	$\pm 20\%$	80%	± 0.0	± 0.0	± 0.0	± 0.0	± 0.1	± 0.1	± 0.1	± 0.1
Water salinity	± 2 psu	28 psu	± 0.0	± 7.3	± 0.0	± 7.3	± 0.0	± 7.8	± 0.0	± 7.5

⁽¹⁾ First and second winter wind regime

Table 2. Influence of uncertainties in the meteorological dataset and empirical coefficients on modelled sea ice production and salt rejection

production and salt rejection to uncertainties in the meteorological dataset and empirical coefficients is summarized in Table 2. A comprehensive chart is attached to the Appendix.

[66] Disparities in the recorded wind direction would necessitate the model input φ_0 to differ. A φ_0 variation of $\pm 10^\circ$ results in an average model error of $\pm 5.2 \%$ for thin ice, $\pm 3 \%$ for frazil ice (see Table in Appendix) and $\pm 5.5 \%$ for the total ice production and salt flux.

[67] Since even small variations in the thin ice drift factor B_i of up to $\pm 0.5 \%$ lead to a final ice production error of $\pm 23 \%$, B_i is based on an ice tracking approach (see section 4.1.2). The open water width remains unaffected by fluctuations in B_i , and so does the frazil ice production. Disparities in b_i however, influence both, the thin ice ($\pm 3.5 \%$) and frazil ice productivity ($\pm 22.8 \%$), and reflects in total ice production and salt flux by $\pm 12.1 \%$ and $\pm 7.6 \%$, respectively.

Besides frazil ice drift and thin ice drift velocity, another parameter with a major effect on ice partition is the frazil collection thickness h_c . Because the frazil accumulation depths underlie ocean and atmospheric dynamics, we vary h_c between 15 cm and 7 cm. Assuming h_c to be constant causes a total ice production and salt flux error of $\pm 12.2 \%$. If h_c is taken as a logarithmic function that increases with wind velocity, the total error in ice production is around $\pm 12.5 \%$. Equation 5 does not include the $\Delta h_f / h_c$ ratio.

[68] An average uncertainty of $\pm 2^\circ\text{C}$ in recorded air temperatures between the Dunai Station and the SWNS polynya (T_{Dunai} to T_{WNS}) causes the total ice production to vary by $\pm 7.2 \%$. This assumption affects all three models equally. Next we induce a wind velocity deviation of ± 0.5 m sec⁻¹ in the

polynya region. This results in an average sea-ice growth error of $\pm 6.9 \%$ and the final salt flux to differ by $\pm 12.2 \%$. The open water model with the freeze-up threshold is found to be more sensitive to wind velocity variations (error in ice accumulation $\pm 10.1 \%$), since it suggests the wind to be the only driving force for the opening and closing of the open water area.

[69] Furthermore, we evaluate the model response to variations in empirical coefficients, assisting heat flux computations. According to *Haarpaintner et al.* [2003], the bulk transfer coefficient for turbulent heat fluxes between atmosphere and thin ice or water differs in the literature by about 50 %. Varying the bulk transfer coefficient by $\pm 0.5 \times 10^{-3}$ results in a final average model error of $\pm 3 \%$ for thin ice, $\pm 2.7 \%$ for frazil ice (Table in Appendix) and $\pm 3.4 \%$ for total ice production and salt flux, in all three models. The sensitivity of the models to variations in cloud cover (± 0.2) and relative humidity ($\pm 20 \%$) is tested and found to be insignificant.

[70] Although the open water widths model performance (r) of equation 5 is significantly better, its final ice and salt flux estimations are strongly affected by disparities in the meteorological dataset and empirical coefficients. The implementation of h_c in the open water model improves its sensitivity to external parameters. The open water model with a constant h_c shows the lowest overall sensibility, but differs only slightly from the usage of a wind-depended logarithmic h_c .

6. Discussion

[71] The total ice production of the SWNS polynya was calculated based on a method of *Haarpaintner et al.*, [2001]. A description of the applied algorithms for width modelling and ice growth computation is given in chapter 4. The objective of this study is to model the amount of ice produced and brine rejected in the SWNS polynya during winter 2003/2004 and link it to the long-term average salinity variance of the south-eastern Laptev Sea. Our calculations are limited to thin and frazil ice growth in the active polynya zone.

6.1 Total polynya width algorithm

[72] The algorithm (equation 3) developed by *Haarpaintner et al.* [2001], was successfully applied to the SWNS polynya. Since the model approach is highly empirical, it can be easily tuned to the ASAR measurements. The high correlation coefficient we obtained between observed and modelled total widths (Figure 15) shows that the width model, originally developed to study the Storfjorden polynya, is transferable to the eastern Laptev Sea.

[73] On some images, the transition zone between thin ice and first year ice/pack ice is distorted, so that sometimes the absolute accuracy of the width measurements varies by several kilometres. To calibrate the polynya model, we excluded measurements of low precision. Figure 27 illustrates the problem of polynya widths interpretation. The left ASAR image was taken on February 27. Bright banded zones of newly formed ice can be seen, each band indicative of different stages of development and ice thickness [Haas *et al.*, 2004a]. During the next 2 weeks the polynya extent is still increasing, while the backscatter of the former thin ice region darkens through changes of ice properties. On March 11, 2004 (Figure 27b) it is difficult to extract a reliable width. The former downwind polynya extend is still visible in the image, but since ice thickening took place, the smoothed new ice layer can not be referred as thin ice without greatly overestimating ice production. In this case, we defined the break-off event with the narrow thin ice zone along the fast ice edge as the active polynya zone (indicated by white arrows).

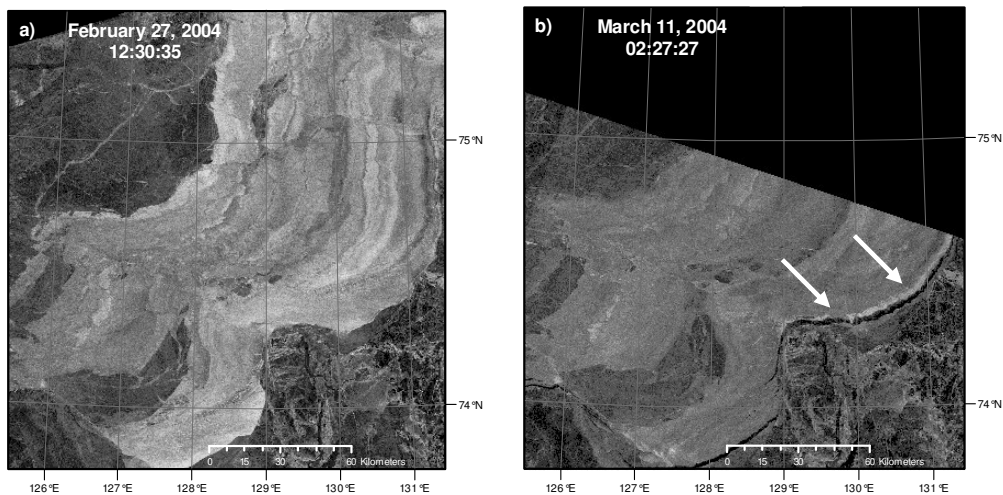


Figure 27. WSM ENVISAT ASAR images of the SWNS polynya taken on February 27, and March 11 2004.

6.2 Open water width algorithm

[74] The general performance of the open water models is weaker. Although equation 4 (with constant h_c) has the lowest correlation coefficient between modelled and observed open water widths, it is least sensitive to meteorological uncertainties. The use of a logarithmic function for frazil ice accumulation thickness does not significantly improve model output and sensitivity. Furthermore, we displaced the consolidation thickness in equation 4 with a freeze-up threshold and $A(\varphi_n - \varphi_o)$ factor (equation 5). This somehow improves the widths accuracy, but the model output becomes more

susceptible to wind velocity variations, since it suggests the wind to be the only driving force for opening and closing of open water areas.

[75] In addition, a reliable extraction of open water zones from the ASAR imagery is not always guaranteed. Since the measurement rate is undersampled, a systematic validation of the applied open water models is more difficult. As discussed in section 4.1.1, wind speeds greater than about 5-10 m s⁻¹ creates Langmuir circulations, which provide hints for the presence of open water. Under calm wind conditions however, the backscatter of open water and nilas ice overlaps, limiting the use of WSM products. The higher spatial resolution of APP products and the VV/HH co-polarisation certainly burrows additional potential. Furthermore, the use of ASAR/AVHRR composites from near-concurrent images proved its capability for open water localisation. However, the implementation of AVHRR data is restricted by its low resolution and the necessity of cloud free conditions.

[76] According to *Dmitrenko* [2005], the general character of the circulation measured along transects at the fast ice margin is most likely due to salinization of the surface water caused by ice formation in the flaw polynya. The consideration of tidal forcing in the Eastern Laptev Sea would eventually improve the accuracy of the simulated open water evolution. Since currents contribute to ice motion and frazil ice accumulation, we extended equation 4 by a current component. Together with ice thickness, velocity and flow direction of surface currents were recorded by ADCP in the WNS polynya. Equation 10 implements the current information by assuming the downwind herded frazil ice to be a function of surface currents ($V_{current\ drift}$) and wind stress ($U_{ice\ drift}$):

$$R_{OW} = R_{OW(n-1)} \cdot \left(1 - \frac{\Delta h_f}{h_c} \right) + (W_1 \cdot U_{ice\ drift} + W_2 \cdot V_{surface\ drift}) , \quad (10)$$

$$W_1 + W_2 = 1 ,$$

$$U_{ice\ drift} = (b_i \cdot U \cdot \cos(\varphi_n - \varphi_o) \cdot \Delta t) ,$$

$$V_{current\ drift} = (V \cdot \cos(\delta_n - \delta_o) \cdot \Delta t) ,$$

where W_1 and W_2 are constant factor chosen during model calibration, that weight the effect of currents and winds on open water formation. The sum of W_1 and W_2 is 1. V is the recorded current drift velocity (ADCP), δ_n is the recorded current direction and δ_o represents the dominant current direction. So far, the extension of the open water algorithm by a current factor gives only reasonable results. We found the correlation coefficient between observed and modelled widths to be lower than the accuracy of equation 4. However, since the effect of surface circulation on frazil ice accumulation is still ill-understood, it is difficult to empirically include it in the model.

[77] Following Pease, the velocity of frazil ice drift in percent of wind speed (b_i) is supposed to be 1 % higher than the thin ice drift rates, although it is likely that B_i and b_i are not constant but vary with the geometry of the fast ice edge and ice thickening. A more accurate b_i constant might also contribute to an improvement of the open water model performance. Another model simplification is the idealized accumulation of frazil ice against the downwind polynya edge. The frazil ice formed in the water body is assumed to instantaneously pile up. To overcome this deficiency, *Ou* [1988] develops a model incorporating a finite frazil ice drift rate together with time-varying winds and air-temperature [*Marqueda et al.*, 2005].

6.3 Polynya length

[78] A number of recent polynya studies have addressed axial length-variation scenarios with models of various complexities [*Biggs et al.*, 2003]. The simple model we applied to the eastern Laptev Sea neglects polynya lengths variations since AVHRR and ASAR data indicates no serious perturbations in length scale during winter 2003/2004 in our study area.

6.4 Ice growth modelling

[79] Thin ice growth was calculated based on Stefan's law (equation 9), neglecting an insulating snow coverage. However, it is likely that interim snow fall events lead to a snow cover of the thin ice area, affecting the ice thickness evolution substantially. We therefore examined the effect of intermediate snow coverage on the thin ice productivity. Figure 28 presents the negative impact of an insulating snow layer on the total thin ice growth (total thin ice reduction in percent) over the proportion of thin ice that might have been covered with snow. Assuming only 15% of the total accumulated thin ice to be covered with a snow deposition of 1.1 cm (10 % of h_c), results in a thin ice flux reduction of 4 %. Unfortunately, the lack of precipitation data for winter 2003/2004 does not allow consideration of snow fall in the model.

[80] The surface energy budget of the SWNS polynya and the frazil ice accumulation in the open water area was investigated through the combination of meteorological data and simple physical models. The net heat flux curve is characterised by periods of high heat fluxes, interspersed with more quiescent episodes. The sensitivity study in section 5.1 examines the effect of disparities in the bulk transfer coefficient and the recorded wind and temperature data on the modelled Q_{net} . As discussed, oscillations in heat flux are almost exclusively associated with changes in air temperatures and wind speed. However, we must not forget that as the near surface air crosses the polynya, it is gradually warmed and moistened. Therefore, the sensible and latent heat flux decreases with distance from the

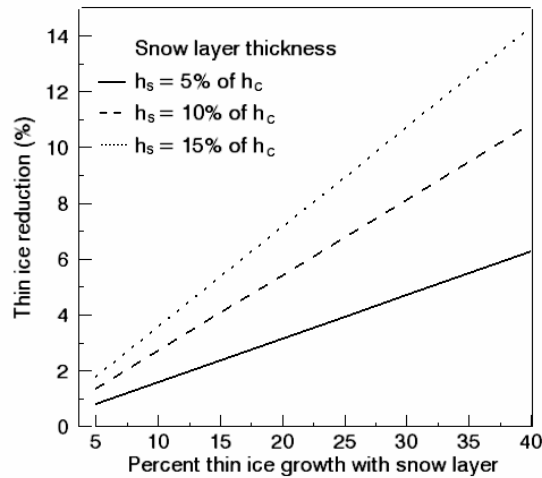


Figure 28. Effect of a snow coverage (percent thin ice growth with snow layer) on the modelled thin ice production (thin ice reduction in percent) for different snow thicknesses h_s (percent of h_c).

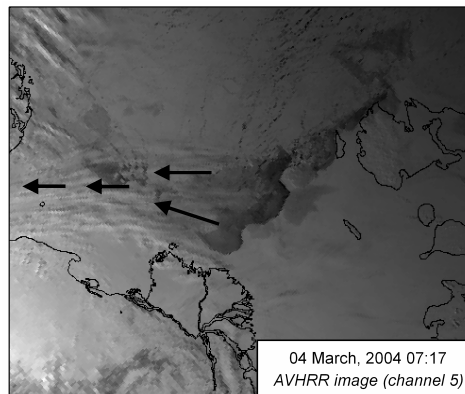


Figure 29. AVHRR image (channel 1) of the south-eastern Laptev Sea, taken on March 4, 2004. Upward rising clouds (arrows), originating from moisture-laden air warmed by the ocean, cool and condensate instantly.

upwind fast ice edge. *Renfrew et al.* [2000] estimate the rate of heat flux to decrease in the order of 20% over fetches of 50 km. A crude parameterization of this effect would certainly improve the accuracy of the modelled frazil ice production. Consequently, we suppose the frazil ice accumulation in the SWNS polynya to be overestimated by 15%. Figure 29 presents an AVHRR image (channel 1) taken on March 04, 2004, showing a convective cloud downwind (to the East) of the SWNS polynya. The upward rising clouds, originating from the moisture-laden air warmed by the ocean, cool and condensate instantly. The process of thermal internal boundary layer (IBL) formation over polynyas is described in detail by *Renfrew et al.*, [2000, 2002] and *Morales Maqueda et al.*, [2004]. Table 3

(reprinted from *Morales Maqueda et al.* [2005]) displays a compilation of net turbulent and radiative heat fluxes over selected polynyas reported in the literature and compares it to our computations for the SWNS polynya in winter 2003/2004.

Polynya(s)	Observation Period	Area 1000 km ²	$Q_{\text{turbulent}}$ W m ⁻²	Averaged Net Heat Flux	Rad. Flux W m ⁻²	Source
Bennet Island	18 February 1983	0.3-0.375	-458		-105	<i>Dethleff, [1994]</i>
Dundas Island	March 1980	1	-270		-60	<i>Topham et al., [1983]</i>
			-270			<i>Den Hartog et al., [1983]</i>
Okhotsk Sea coast (southwest)	December 1987–1982	25 ^b	-471		-94	<i>Alfulitis et al., [1987]</i>
Okhotsk Sea coast	Januar –March 1990–1995	25.4 ^b		-256		<i>Martin et al., [1998]</i>
Queen Maud Land coast	December 1986 to February 1987	...	3		142	<i>Ramesh Kumar et al., [1989]</i>
Ronne Ice Shelf	winter 1992-98	4.893	-272		-47	<i>Renfrew et al., [2002]</i>
Ronne Ice Shelf	summer 1992-98	36.2	-1		160	<i>Renfrew et al., [2002]</i>
St. Lawrence Island	Winter 1981	...		-535		<i>Schumacher et al., [1983]</i>
St. Lawrence Island	February 1982-83	...	-192/-412 ^c		-79/91 ^c	<i>Pease, [1987]</i>
Northeast Water	July–August 1992	10-18	-7.1 ^d		80.9 ^d	<i>Minnett, [1995]</i>
Northeast Water	Spring 1993	...	-31		195	<i>Schneider et al., [1995]</i>
Storfjorden	7 March 1998	6	-300		-100	<i>Haarpainmer et al., [2001]</i>
Terra Nova B.	May–September	1	-790		-38	<i>Kurtz et al., [1985]</i>
Weddel Sea coast (60°W-20°E)	May–October 1992	15	-100/-300 ^e		50/-100 ^e	<i>Markus et al., [1998]</i>
SWNS polynya	February-March2004	18; 1.3 ^b	-342	-482		

^a Negative values indicate heat loss from the polynya to the atmosphere

^b Value does not include area of thin ice

^c Values are for the 1982 and 1983 events, respectively

^d Values are weighted by observed ice cover

Table 3. Net turbulent and radiative heat flux in selected polynyas ^a (reprinted from *Morales Maqueda et al.*, [2004]) compared to the SWNS polynya.

6.4 Ice and salt flux

[81] The interannual and seasonal variability of sea-ice in the Laptev Sea has been recently studied in detail by *Bareiss et al.* [2005]. Satellite derived passive microwave data (Sensor Microwave Imager SSM/I) from 1997 through 2002 was used to monitor the evolution of polynya open water areas with a simple threshold method. According to *Bareiss et al.*, the average open water area in the entire WNS polynya is 4×10^3 km² in winter. Maximum polynya events, covering up to 25% of the eastern Laptev Sea (73×10^3 km²) have been observed in the past 24 years. However, sensor characteristics of the passive microwave radiometer and deficiencies in the used sea-ice concentration algorithms to discriminate unambiguously between thin ice and open water, limit the accuracy of the obtained mean seasonal statistics for flaw polynyas in the Laptev Sea. *Winsor et al.* [2000] investigated Arctic polynyas during 39 winter seasons from 1958 to 1997 by means of a large scale polynya model. A mean width of 3.4 km and an average ice production of 4 km³ was found for the Laptev polynyas. This corresponds to an ice production of 14.2 m (around 5 m higher than our computation). Based on the hydrographical model of *Dmitrenko et al.*, the total ice production in the Laptev Sea is around

3-4 m. Any discrepancies in the literature according the WNS polynya extent, frequency and productivity can be partially explained by the use of different sensor systems, models, observation periods and alternating definitions for the term "active polynya". However, since we only examined a small fraction of the Laptev polynyas, it is difficult to directly compare it to earlier studies.

[82] The final amount of salt released depends on the initial water salinity [Haarpaintner *et al.*, 2001]. We assumed the average long-term salinity measurements obtained from hydrological data, taken between 1979 and 1999 in the south-eastern Laptev Sea, to be representative for situation in winter 2003/2004. A linear increase of the surface salinity throughout the season due to intensive ice production was not taken into account. Since 69 % of the initial water salinity is released by spontaneous salt rejection, frazil ice formation (high potential productivity, Figure 23) plays a major role in adding salt to the surface layer. However, the general calm wind condition in the Lena delta (on average 4.3 m sec^{-1}) limits the development of large open water areas. Therefore, we assume the thin ice area to essentially govern brine rejection in the south-eastern Laptev Sea. Because continuous salt rejection during thin ice growth, aging and cooling (10% of the initial salinity) is slower and distributed over a larger area, we found the total amount of salt produced to be less than expected. Following *Dimitrenko et al.*, [2005], the probability for convective mixing down to the seafloor in the eastern Laptev Sea does not exceed 20 %, which can be partially explained by our modelled high thin ice fraction.

[83] To evaluate the effect of salt released on the initial water salinity, the total ice production was calculated over an area of 25,000 km² (maximum extent of the SWNS polynya), roughly estimating continuous pack ice and fast ice growth. Assuming a mean water depth of 35 m, the water volume is around $8.75 \times 10^{11} \text{ m}^3$. Neglecting observed strong surface currents [Dimitrenko *et al.*, 2005] dispersing the outflow of brine enriched surface waters, 2086 Mt of salt (including pack ice and fast ice rejection) would temporarily increase the overall water salinity in the polynya by 2.4 psu between January and June. Based on average long term salinity records, *Dimitrenko et al.* [2005] found the local maxima in salinity variance to be coincident with the long-term mean location of the flaw polynya. A winter variance of 3.5 - 4.2 psu was measured at the surface northward the fast ice edge. Since the observed strong vertical density stratification in the polynya region and the calculated low convective mixing probability restricts a salinity increase to upper layers, we suppose the distribution of modelled salt flux to be limited to 15 m depth [Dimitrenko *et al.*, 2005]. Consequently, the surface salinity in the polynya area would increase by 4.6 psu. Neglecting any advection, this value slightly exceeds the salinity deviation range of 3.5 – 4.2 psu recorded by *Dimitrenko et al.* [2005]. However, surface currents from outside the polynya region renew water masses and reduce the continuous water salinity increase during winter. Therefore we used ADCP surface current velocity data to account for the effects of currents on the salinity evolution of the upper water layer. An implementation into our

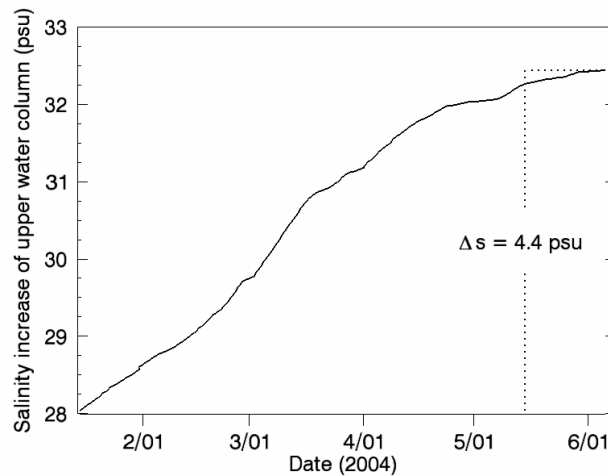


Figure 30. Seasonal evolution of salinity (in psu) in the upper water layer of the SWNS polynya ($8.75 \times 10^{11} \text{ m}^3$), taking into account water mass fluxes recorded by ADCP.

calculations reduces the seasonal salinity variance by 0.2 psu to 4.4 psu (Figure 30). Since current records are based on a single point observation and the initial salinity at the origin of the surface current is unknown, the computed salinity increase in the polynya area is only a crude estimation. However, the results show that the modelled salt flux for the SWNS polynya matches field observations and may provide more accurate input for complex ocean and convection models.

7. Conclusion and future direction

[84] The WSM and APP ENVISAT ASAR images taken over the south-eastern Laptev Sea between November 2003 and June 2004 and the polynya flux model, developed by *Haarpaintner et al.* [2001], provides new detailed insight into sea-ice regime dynamics and ice and salt fluxes of the southern West New Siberian polynya.

[85] The model calculates the width of open water zones and the total polynya width separately, using two different algorithms, driven by meteorological data recorded at a nearby weather station. Because the agreement between modelled and measured total polynya width was very high, we assume that opening and closing of the SWNS polynya can be expressed as a function of wind velocity and direction. The performance of the open water width algorithm was generally weaker. Therefore we tested three slightly different models, with correlation coefficients varying between 0.65 and 0.75. A sensitivity study showed that the approach first formulated by *Pease* [1987], is least sensitive to disparities in the meteorological datasets and the parameters assisting heat flux computations. To derive the open water and the thin ice area, the modelled thin ice widths and open

water widths were multiplied with the length of the study area (195 km). The computation of frazil ice formation in the open water area was based on the net surface heat balance and continuous thin ice growth in the thin ice area was assumed to follow Stefan's law.

[86] A total ice volume of 51 km³ in thin ice and 15 km³ in open water areas was generated in the SWNS polynya between January 7, and June 4, 2004. This corresponds to an average ice production of 9.6 m m⁻². A period of strong persistent eastern winds between February and April contributed significantly to ice production and salt rejection. A maximum extent of around 129 km could be observed at the beginning of March. The modelled average polynya width was around 36 km.

[87] The accumulated salt rejection from both, ice formation and aging processes during the observation period was 1506 Mt. Considering additional continuous pack ice and fast ice growth in an area of 25,000 km² and water mass exchange, induced by strong surface currents, the surface salinity increased by approximately 4.4 psu between January and June. This corresponds well with the salinity deviation range of 3.5 – 4.2 psu for the WNS polynya location, derived from long-term average salinity records by *Dmitrenko et al.* [2005]. According to their calculations, the probability for convective mixing down to the seafloor in the south-eastern Laptev Sea does not exceed 20%. Modelled high thin ice fraction and mostly very little open water during winter 2004 partially explain the absence of mixing events, since continuous salt rejection during thin ice growth, aging and cooling is slower and less concentrated in space.

[88] The good agreement between the modelled increase in water salinity and long-term salinity field records shows the potential of the *Haarpaintner* model for salt and ice flux computations in flaw polynyas. However, the SWNS polynya must be studied in more detail over next winter periods. As already discussed by *Haarpaintner et al.* [2001], a better quantification of open water areas in the SAR imagery is necessary. We demonstrated the capability of cross-polarization ratios for automatic polynya segmentation and AVHRR/ASAR composites for open water identification. The implementation of currents, affecting open water formation in the algorithm would certainly contribute to the model sensitivity and model cross-error. Furthermore, we expect the use of precipitation data and the consideration of heat flux decrease over open water areas with distance from coast, to improve the applied ice growth algorithms.

[89] To study the effect of varying polynya driving forces on the ice, salt and heat budget of the SWNS polynya require the studies such as this one be extended, with a combination of ground-based and remote-sensing measurements. Therefore, three winter expeditions and new mooring deployment in the region north of the Lena Delta are planed until 2008. A helicopter based electromagnetic induction device [*Haas, 2004b*] will provide ice thickness variability information in the polynya region to validate thin ice thickness data derived from AVHRR [*Drucker et al., 2004*] and radar [*Kern et al., 2006*] imagery, contributing to the calibration of the flux model. The importance of the amount

of ice and salt produced as compared to the local circulation system and the halocline of the Arctic Ocean, still needs to be established.

Acknowledgements

[90] First of all, I would like to gratefully acknowledge the enthusiastic supervision of Dr. Christian Haas during my time at AWI. Secondly, I wish to thank Dr. Wolfgang Dierking, Prof. Gerard Govers, my promoter at the K.U.Leuven, and Jon Harbor, my co-promoter at the University Purdue. I thank the Arctic and Antarctic research Institute in St. Petersburg for providing us with meteorological data. Satellite data were obtained through ESA Project EO-500 "Formation, transport and distribution of sediment-laden sea-ice in the Arctic Shelf seas". Special thanks to the University Trier for AVHRR processing. The comments of Jens Hoesemann, Joao Marcelo Absy, Michael Fuelberth and Jos van Orshoven are gratefully acknowledged. I am deeply indebted to Thomas Busche, for teaching me the basics in programming and writing an EASY script for image registration. Finally I would like to thank Alex for her loving support and my parents Monika and Wolfgang for supporting me while I was working on this study.

References

- Alexandrov, V., Martin, T., Kolatschek, J., Eicken, H., Kreyscher, M. and Makshtas, A.P., "Sea ice circulation in the Laptev Sea and ice export to the Arctic Ocean: Results from satellite remote sensing and numerical modelling." *Journal of Geophysical Research*, 2000, 105(C7), pp. 17,143-17,159.
- Barber, D. G., Yackel, J. J. and Hanesiak, J. M., "Sea Ice, RADARSAT-1 and Arctic Climate Processes: A Review and Update." *Canadian Journal of Remote Sensing*, 2001, (16), pp. 51-61.
- Bareiss, J. and Görden, K., "Spatial and temporal variability of sea ice in the Laptev Sea: Analysis and review of satellite passive-microwave data and model results, 1997 to 2002." *Global and Planetary Change*, 2005, 48pp. 28-54.
- Belchansky, G. I., Douglas, D. C., Mordvintsev, I. N. and Platonov, N. G., "Estimating the time of melt onset and freeze onset over Arctic sea-ice area using active and passive microwave data." *Remote Sensing of Environment*, 2004, 92pp. 21-39.
- Biggs, N. R. T., Morales Maqueda, M. A. and Wilmot, A. J., "Polynya flux model solutions incorporating a parameterisation for the collection thickness of consolidated new ice." *Journal of Fluid Mechanics*, 2000, 408pp. 179-204.
- Cavalieri, D. J., Burns, B. A. and Onstott, R. G., "Investigation of the Effect of Summer Melt and the Calculation of Sea Ice Concentration Using Active and Passive Microwave Data." *Journal of Geophysical Research*, 1990, 95(C4), pp. 5359-5369.
- Dieckmann, H. S. and Helmer, H., *The Importance of Sea Ice: An Overview*. 2002.
- Dmitrenko, I.A., Tyshko, K.N., Kirillov, S.A., Eicken, H., Hölemann, J. and Kassens, H., "Impact of flaw polynyas on the hydrography of the Laptev Sea." *Global and Planetary Change*, 2005, 48pp. 9-27.
- Dokken, S. T., Winsor, P., Markus, T., Askne, J. and Björkl, G., "ERS SAR characterization of coastal polynyas in the Arctic and comparison with SSM/I and numerical model investigation." *Remote Sensing of Environment*, 2002, 80pp. 321-335.
- Drucker, R., Martin, S. and Moritz, R., "Observation of ice thickness and frazil ice in the St. Lawrence Island polynya from satellite imagery, upward looking sonar, and salinity/temperature moorings." *Journal of Geophysical Research*, 2003, 108(C5), pp. 18, 1-18, 17.
- Eicken, H., Reimnitz, E., Alexandrov, V., Martin, T., Kassens, H. and Viehoff, T., "Sea-Ice processes in the Laptev Sea and their importance for sediment transportation." *Continental Shelf Research*, 1997, 17(2), pp. 205-233.
- Eicken, H., Blahak, U., Diekring, W. and Dmitrenko, I., "Spatial and temporal variability of SAR backscatter signatures of coastal sea-ice types off the Lena River Delta (Laptev Sea)." *IEEE*, 1999, 0-7803-5207-6/99.
- Eicken, H., *Sea Ice*. Oxford: Blackwell Publishing, 2003.
- Eicken, H., Dmitrenko, I., Tyshko, K., Darovskikh, A., Dierking, W., Blahak, U., Groves, J. and Kassens, H., "Zonation of the Laptev Sea landfast ice cover and its importance in a frozen estuary." *Global and Planetary Change*, 2005, 48pp. 55-83.

- ESA, *CMOD4 Model Description.*, 1993.
- ESA, *Absolute Calibration of ASAR Level 1 Products generated with Pf-ASAR.* Frascati, Italy, 2004a.
- ESA, *Product Handbook*, Frascati, Italy, 2004b.
- Haarpainter, J., Gascard, J. and Haugan, M., "Ice production and brine formation in Storfjorden, Svalbard." *Journal of Geophysical Research*, 2001, 106(C7), pp. 14,001-14,013.
- Haas, C. and Eicken, H., "Interannual variability of summer sea ice thickness in the Siberian and central Arctic under different atmospheric circulation regimes." *Journal of Geophysics Research*, 2001a, 106(C3), pp. 4449-4462.
- Haas, C., Thomas, D. and Bareiss, J., "Surface properties and processes of perennial Antarctic sea ice summer." *Journal of Glaciology*, 2001b, 47(159), pp. 613-624.
- Haas, C., Dierking, W., Busche, T. and Hoelemann, J., *ENVISAT ASAR Monitoring of polynya processes and sea ice production in the Laptev Sea.* Alfred-Wegener Institute, Bremerhaven, Germany, 2004a.
- Haas, C., *Arctic Sea Ice Thiickness Variability in the 1990s Retrieved From EM Sounding.* Alfred-Wegener Institute, Bremerhaven, Germany, 2004b.
- Hall, D. K., *Remote Sensing of Ice and Snow.* London, New York: Chapman and Hall, 1985.
- Harms, I. H., Karcher M. J.; Dethleff, and Dethleff, D., "Modelling Siberian river runoff - implication for contaminant transport in the Arctic Ocean." *Journal of Marine Systems*, 2000, 27pp. 95-115.
- Jeffries, M., Morris, K. and Liston, G., *ERS-1 SAR monitoring of ice growth on shallow lakes to determine water depth and availability in N.W. Alaska*, TUD Lyngby, Denmark: ESA, 1996.
- Kaleschke, L., *Fernerkundung des Meereises mit passiven und aktiven Mikrowellensensoren.*, 2003.
- Lebedev, V. L., "Maximum size of a wind-generated lead during sea freezing." *Oceanology*, 1968, 8pp. 313-318.
- Livingstone, C. E., Onstott, R. G., Arsenault, L. D., Gray, A. L. and Singh, K. P., "Microwave Sea-Ice Signatures Near the Onset of Melt." *IEEE*, 1987, 25(2), pp. 174-187.
- Macdonald, R. W., Harner, T. and Fyfe, J., "Recent climate change in the Arctic and its impact on contaminant pathways and interpretation of temporal trend data." *Science of the Total Environment*, 2005, 342(4 [3]), pp. 5-86.
- Mahafza, B., *Introduction to radar analysis.* Huntsville, Alabama: CRC, 1998.
- Martin, S. and Cavalieri, D. J., "Contribution of the Siberian shelf polynyas to the Arctic Ocean intermediate and deep water, *Journal of Geophysical Research*, 94, pp. 12,725-12,738.
- Martin, S., *Polynyas.* Seattle, 2001.
- Massom, R., *Satellite Remote Sensing of Polar Regions.* Lewis Publisher, 1991.

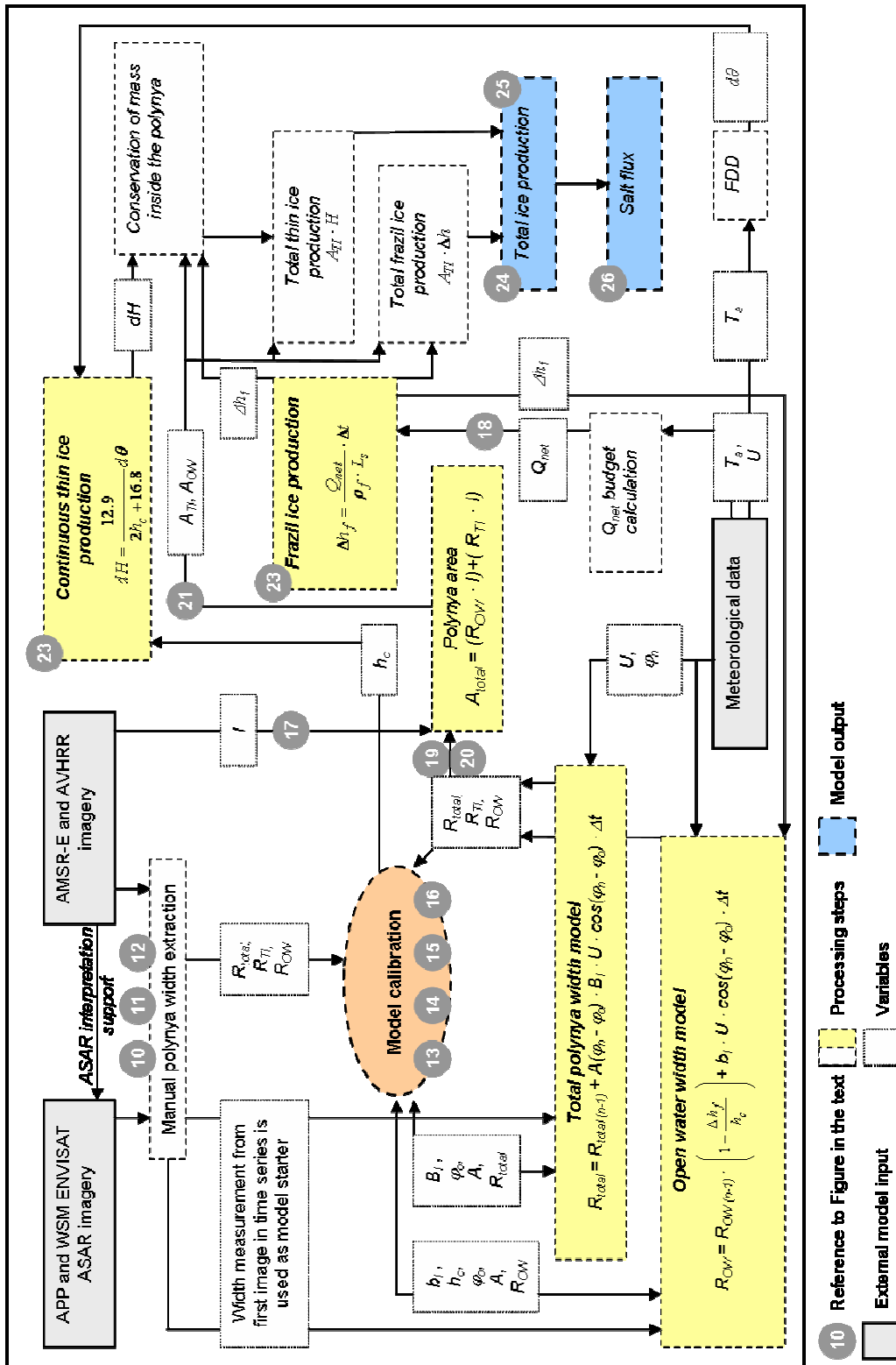
- Maykut, G. A., The surface heat and mass balance, *The geophysics of sea ice*, Martinus Nijhoff Publ., Dordrecht
- Morales Maqueda, M. A., Wilmot, A. J. and Biggs, N. R. T.. "Polynya dynamics: A review of observation and modelling." *Review of Geophysics*, 2004, 42(2002RG0001116).
- Ou, H. W., "A time-dependent model of a coastal polynya." *Journal of Physical Oceanography*, 1988, 18pp. 584-590.
- Pease, C. H., "The size of wind-driven coastal polynyas." *Journal of Geophysical Research*, 1987, 92pp. 7049-7059.
- Reimnitz, E., Dethleff, D. and Nürnberg, D., "Contrasts in Arctic shelf sea-ice regimes and some implications: Beaufort Sea and Laptev Sea." *Marine Geology*, 1994, 28pp. 179-210.
- Renfrew, I. A. and John, C. K., "A simple model of the convective internal boundary layer and its application to surface heat flux estimates within polynyas." *Boundary-Layer Meteorology*, 2000, 94pp. 335-356.
- Renfrew, I. A., King, J. C. and Markus, T., "Coastal polynyas in the southern Weddel Sea: Variability in the surface energy budget." *Journal of Geophysical Research*, 2002, 107(C6), pp. 3063.
- Rigor, I. G. and Colony, R. L., "Sea-ice production and transport of pollutants in the Laptev Sea, 1997-1993." *Science of the Total Environment*, 1997, 202pp. 89-110.
- Rivera, J., Karabanov, E. and Williams, D., "Lena River discharge events in sediments of Laptev Sea, Russian Arctic." *Estuarine, Coastal and Shelf Science*, 2005, 66pp. 185-196.
- Shcherbina, A., *Ice thickness profiling from the moorings' data*. University of California, Physical Oceanography Research Division, 2002, http://www-pord.ucsd.edu/~ashcherbina/ice_profiling.pdf
- Sandven, S., Johannessen, O., Miles, M., Pettersson, L. and Kloster, K., "Barents Sea seasonal ice zone features and processes from ERS 1 synthetic aperture radar: Seasonal Ice Zone Experiment 1992." *Journal of Geophysical Research*, 1999, 104(C7), pp. 15,843-15,857.
- Sandven, S., *Sea ice observed from space*. Bergen, Norway, 1999.
- Sandven, S., Dalen, O., Lundhaug, M., Kloster, K., Alexandrov, V.Y. and Zaitsev. L.V., "Sea ice investigation in the Laptev Sea area in late summer using SAR data." *Canadian Journal of Remote Sensing*, 2000, 27(5), pp. 502-514.
- Sharma, P., *Effect of meteorological condition on polynya formation and processes*. 2003.
- Small, D., Rosich, B. and Meier, E., Nuesch, D.. *Geometric Calibration and Validation of ASAR Imagery*. Frascati, Italy: European Space Agency, 2005.
- Ulaby, F. T., Moore, R. K. and Fung, A. K., *Microwave Remote Sensing: From Theory to Applications*. Artech House, INC, 1986.
- Ulander, Lars M. H., "Radar Remote Sensing." *European Space Agency*, 1991.

- Wegner, C., Hoelemann, J. A., Dmitrenko, I., Kirillov, S. and Kassens, H., "Seasonal variations in Arctic sediment dynamics - evidence from 1-year records in the Laptev Sea (Siberian Arctic)." *Global and Planetary Change*, 2005, 48pp. 126-140.
- Winebrenner, D. P., Nelson, E. D. and Coloy, R., "Observation of melt onset on multiyear Arctic sea ice using ERS 1 synthetic aperture radar." *Journal of Geophysical Research*, 1994, 99(C11), pp. 22,425-22,441.
- Winsor, P. and Björk, G., "Polynya activity in the Arctic Ocean from 1958 to 1997." *Journal of Geophysical Research*, 2000, 105(C4), pp. 8789-8803.
- World Meteorological Organization, "WMO sea-ice nomenclature." *Technical publication* , 1970, (WMO 259 TP 145 1970), pp. 2-7.
- Yackel, J. J. and Barber, D. G., "Melt ponds on sea ice in the Canadian Archipelago 2. On the use of RADARSAT-1 synthetic aperture radar for geophysical inversion." *Journal of Geophysical Research*, 2000, 105(C9), pp. 22,061-22,070.
- Zakharov, V. F., "The role of flaw leads off the edge of fast ice in the hydrological and ice regime of the Laptev Sea." *Oceanology*, 1966, 6pp. 815-821.

Appendix

<i>A1. Figure: Model work flow</i>	58
<i>A2. Table: Sensitivity study</i>	59

Appendix A1 Model work flow



Appendix A2 Sensitivity study

Parameter	Variation	PEASE model with log. h_e (Equation 4)						Freeze-up threshold model (Equation 5)						Average (columns 1-3)			
		Prasil ice prod. (%)	Thin ice growth (%)	Ice volume (%)	Salt release (%)	Prasil ice prod. (%)	Thin ice growth (%)	Ice volume (%)	Salt release (%)	Prasil ice prod. (%)	Thin ice growth (%)	Ice volume (%)	Salt release (%)	Ice volume (%)	Ice volume (%)	Salt release (%)	
φ dominant wind direction	$\pm 10^\circ$	± 3.7	± 6.1	± 5.5	± 5.5	± 3.6	± 5.0	± 4.7	± 4.7	± 1.5	± 4.3	± 3.8	± 3.8	± 3.0	± 5.2	± 4.7	± 4.7
h_i	$\pm 0.5\%$	± 22.7	± 3.7	± 8.3	± 8.2	± 22.7	± 3.8	± 9.7	± 8.2	± 22.7	± 3.1	± 18.3	± 6.3	± 22.7	± 3.5	± 12.1	± 7.6
B_i	$\pm 0.5\%$	± 0.0	± 23.8	± 18.0	± 17.8	± 0.0	± 24.0	± 19.9	± 18.2	± 0.0	± 24.6	± 31.1	± 20.2	± 0.0	± 24.1	± 23.0	± 18.7
h_c	$\pm 4\text{cm}$	± 32.4	± 6.2	± 12.6	± 12.4	± 34.0	± 5.4	± 12.2	± 12.2	± 0.0	± 8.9	± 8.9	± 8.8	± 4.1	± 8.2	± 7.2	± 7.2
T_{down} to T_{water}	$\pm 2^\circ\text{C}$	± 2.0	± 8.1	± 6.6	± 6.5	± 1.3	± 7.7	± 6.2	± 6.2	± 9.0	± 8.9	± 8.9	± 8.8	± 4.1	± 8.2	± 7.2	± 7.2
U_{down} to U_{avg}	$\pm 0.5\text{ m sec}^{-1}$	± 14.5	± 9.7	± 5.8	± 10.7	± 10.0	± 9.1	± 4.9	± 9.3	± 98.9	± 12.8	± 10.1	± 16.7	± 20.5	± 10.5	± 6.9	± 12.2
Bulk transfer coefficient	$\pm 0.5 \times 10^{-3}$	± 2.0	± 2.4	± 2.3	± 2.3	± 0.9	± 2.0	± 1.7	± 1.7	± 18.0	± 3.6	± 6.1	± 6.0	± 7.0	± 2.7	± 3.4	± 3.4
Cloud cover	± 0.2	± 1.0	± 1.0	± 1.0	± 1.0	± 1.1	± 1.1	± 1.1	± 1.1	± 3.8	± 0.8	± 1.3	± 1.3	± 2.0	± 1.0	± 1.1	± 1.1
Relative humidity	$\pm 20\%$	± 0.0	± 0.0	± 0.0	± 0.0	± 0.0	± 0.0	± 0.0	± 0.0	± 0.3	± 0.1	± 0.1	± 0.1	± 0.1	± 0.0	± 0.1	± 0.1
Water salinity	$\pm 2\text{ psu}$	± 0.0	± 0.0	± 0.0	± 7.3	± 0.0	± 0.0	± 0.0	± 7.3	± 0.0	± 0.0	± 0.0	± 7.8	± 0.0	± 0.0	± 0.0	± 7.5